Chemical Science

ROYAL SOCIETY OF CHEMISTRY

EDGE ARTICLE

View Article Online
View Journal | View Issue

Check for updates

Cite this: *Chem. Sci.*, 2025, **16**, 22333

All publication charges for this article have been paid for by the Royal Society of Chemistry

Received 16th August 2025
Accepted 11th October 2025

DOI: 10.1039/d5sc06254c

rsc.li/chemical-science

Open Access Article. Published on 29 October 2025. Downloaded on 2/23/2026 2:13:50 AM. This article is licensed under a Creative Commons Attribution-NonCommercial 3.0 Unported Licence.

# Direct measurement of covalent three-center, two-electron M–H–B bonding in Zr and Hf borohydrides using B K-edge XAS

Hannah M. Hansen,[a] Joshua C. Zgrabik,[a] Peter A. Zacher, III,[a] Jacob J. Schuely,[a] Emily M. Amano,[b] Mai Yer Yang,[a] Daniel K. Unruh,[c] Lucia Zuin,[d] Jason M. Keith *[b] and Scott R. Daly *[a]

Metal borohydride complexes have long been the subject of intense fundamental interest because of their unconventional metal–ligand bonding that occurs *via* three-center, two-electron M–H–B bonds. This type of bonding implies significant delocalization of electron density over all three atoms, but the degree of orbital mixing between the metal and boron has been difficult to assess by direct experimental means. Herein, we demonstrate how ligand K-edge X-ray absorption spectroscopy (XAS) conducted at the B K-edge yields evidence of significant covalent M–H–B bonding with Zr and Hf. To accommodate the B K-edge XAS studies, which were conducted under ultra-high vacuum (<$10^{-8}$ torr), we prepared a series of new $[Zr(RBH_3)_4]$ and $[Hf(RBH_3)_4]$ complexes with substituents that attenuate volatility (R = benzyl, phenyl, mesityl, 2,4,6-triisopropylphenyl, and anthryl). $^{1}H$ and $^{11}B$ NMR spectroscopy, IR spectroscopy, and single-crystal X-ray diffraction (XRD) studies revealed metal and ligand dependent differences in the $BH_3$ chemical shifts that correlate to changes in M–B distances and select B–H vibrational stretching modes. The B K-edge XAS spectra of the Zr and Hf complexes yielded a pre-edge feature that was assigned as B 1s → M–H–B π* based on comparison to time-dependent density functional theory (TDDFT) calculations. The pre-edge transitions appear due to covalent mixing between boron and the metal, thereby demonstrating how B K-edge XAS can provide direct evidence of covalent three-center, two electron M–H–B bonding in borohydride complexes using boron as a spectroscopic reporter.

## Introduction

$[M(BH_4)_4]$ complexes with M = Zr and Hf have inner coordination spheres comprised exclusively of M–H–B bonds and remarkable properties such as high volatility and solubility in non-polar solvents.[1–5] These properties are similar to those observed with simple covalent molecules encountered in organic and main-group chemistry, which prompted Marks and Kolb to refer to these and related d- and f-block complexes as 'covalent' in their seminal review of the field in 1977.[6] Though they were not explicitly referring to the nature of the metal–ligand bonds, group theory assessments at the time revealed the likelihood of significant orbital mixing (*i.e.* covalency)[7] between the metal, hydrogen, and boron orbitals. The M–H–B bonds in these complexes are often described as three-center, two-electron (3c–2e) bonds to emphasize how electron delocalization between boron and the metal is often facilitated by the bridging H atoms.[8] A more refined assessment of this bonding is afforded by molecular orbital theory, which accounts for how electron density can be delocalized over more than three atoms in accordance with the inherent point group symmetry of the complex.[9,10]

Most of the experimental electronic structure assessments in d- and f-block borohydride complexes to date have relied on UV-vis-NIR,[11–16] electron paramagnetic resonance (EPR),[12–14,17] NMR,[18,19] and photoelectron spectroscopy (PES) measurements.[20–23] PES has provided the most orbital specific information about metal–borohydride bonding as this technique quantifies orbital energies by ionizing electrons in occupied molecular orbitals. Moreover, evidence of covalency can be inferred based on branching ratios and changes in occupied MO energies, especially *via* comparison to electronic structure calculations.[21]

An alternative spectroscopic method that could provide a more direct experimental measure of covalency in metal–borohydride bonds is ligand K-edge X-ray absorption spectroscopy (XAS).[24,25] Ligand K-edge XAS uses synchrotron generated

[a]*The University of Iowa, Department of Chemistry, E331 Chemistry Building, Iowa City, Iowa 52242, USA. E-mail: scott-daly@uiowa.edu*

[b]*Colgate University, Department of Chemistry, Hamilton, 13 Oak Drive, New York 13346, USA. E-mail: jkeith@colgate.edu*

[c]*The University of Iowa, Office of the Vice President for Research, 2660 UCC, Iowa City, Iowa 52242, USA*

[d]*Canadian Light Source, University of Saskatchewan, 44 Innovation Place, Saskatoon, SK, Canada*

© 2025 The Author(s). Published by the Royal Society of Chemistry

Open Access Article. Published on 29 October 2025. Downloaded on 2/23/2026 2:13:50 AM. This article is licensed under a Creative Commons Attribution-NonCommercial 3.0 Unported Licence.

light to excite core 1s electrons localized on the ligand atom bound to the metal. Because the orbital selection rule permits 1s → *n*p transitions ($\Delta l = \pm 1$), transitions to unfilled or partially filled molecular orbitals (MOs) containing metal d- or f-character are permitted if ligand *n*p character is also present. Most importantly, the transition intensity is governed by the extent of ligand *n*p character mixing in the wavefunction of the associated orbitals, thereby providing a spectroscopic handle to quantify variations in metal–ligand covalency. These transitions typically appear as pre-edge features in the X-ray absorption near edge structure (XANES; also called NEXAFS) region of the XAS spectrum.

Ligand K-edge XAS has been used successfully to quantify metal–ligand covalency in metal complexes containing a wide range of ligand donors, but to our knowledge, it has never been used to assess covalent bonding with transition metal borohydride complexes. B K-edge XAS and related methods like B K-edge X-ray Raman spectroscopy (XRS) and energy electron loss spectroscopy (EELS) has been used to investigate alkali and alkaline earth metal borohydrides.[26–31] Aside from borohydrides, the only B K-edge data reported on molecular transition metal complexes appears to be XAS and inner-shell electron energy loss spectroscopy (ISEELS) results described for Ni and Fe dicarbollide complexes.[32]

There are several reasons that likely account for the dearth of B K-edge XAS spectra for metal–borohydride complexes. The first reason is that most of these complexes are very air sensitive, making them difficult to handle at synchrotron facilities where XAS measurements are made. $[Zr(BH_4)_4]$ and $[Hf(BH_4)_4]$, for example, are especially pyrophoric and enflame in air. The second reason has to do with the energy of the B K-edge (*ca.* 188 eV). At this energy, any gas or material that could be used to protect the sample would effectively block the beam. This is why B K-edge XAS measurements are carried out in ultra-high vacuum chambers ($<10^{-8}$ torr) on exposed samples. This limitation creates another problem: the ultra-high vacuum environment required for B K-edge XAS data collection precludes the use of volatile metal borohydride complexes like $[Zr(BH_4)_4]$ and $[Hf(BH_4)_4]$, which have vapor pressures of 15 torr at 25 °C.[1]

Here we describe our initial efforts to overcome these issues and collect B K-edge XAS data on homoleptic Zr and Hf borohydride complexes. To address the need for non-volatile complexes, as required to collect data on solid samples in ultra-high vacuum, we first report a series of homoleptic Zr and Hf complexes with trihydroborate ligands containing large benzyl and aryl substituents with intermolecular forces needed to adequately suppress volatility (Fig. 1). We then describe B K-edge XAS and time-dependent density functional theory (TDDFT) analysis of these complexes. The results demonstrate how boron can be used as a spectroscopic reporter of covalent three-center, two-electron M–H–B bonding using ligand K-edge XAS. This is notable given that ligand K-edge XAS has been used almost exclusively to study complexes where the absorbing ligand atom is coordinated directly to the metal.

## Results and discussion

### Synthesis and characterization

The benzyl and aryl boron substituents shown in Fig. 1 were targeted to attenuate the volatility of Zr and Hf complexes for subsequent XAS studies. The trihydroborate starting materials $Li(RBH_3)$ with R = phenyl (Ph),[33] mesityl (Mes),[34] 2,4,6-triisopropylphenyl (Trip),[35] and anthryl (Anth)[36] have been reported previously, and they were synthesized by reduction of the corresponding boronic acid with $LiAlH_4$ in $Et_2O$. The related mixed salt $Li/K(BnBH_3)$ (Bn = benzyl) was synthesized by reducing $K(BnBF_3)$ with $LiAlH_4$ using the method described by Bateman and coworkers.[37] The $^{11}B$ NMR spectra of the trihydroborate salts revealed diagnostic quartets with chemical shifts ranging between $\delta_B$ −26.4 and −32.5 ppm consistent with their literature values.[33–38] The salts were evaporated to dryness and left under dynamic vacuum for extended periods before use, sometimes with heating. We note that they retain small amounts of etherates used in their preparation ($Et_2O$ or thf), but they are not denoted explicitly in the formulas shown throughout.

With the ligand salts in hand, $[M(RBH_3)_4]$ complexes with M = Zr or Hf were prepared by mixing $MCl_4$ with four equivalents of the corresponding ligand salt in pentane (Fig. 1). The complexes were isolated as single crystals by cooling concentrated pentane solutions or vapor diffusion of concentrated

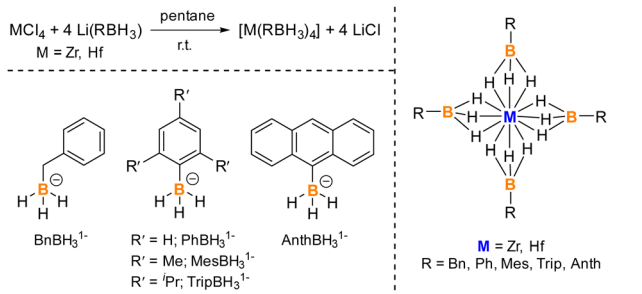


Fig. 1 General synthesis and structures of Zr and Hf trihydroborates investigated in this work.

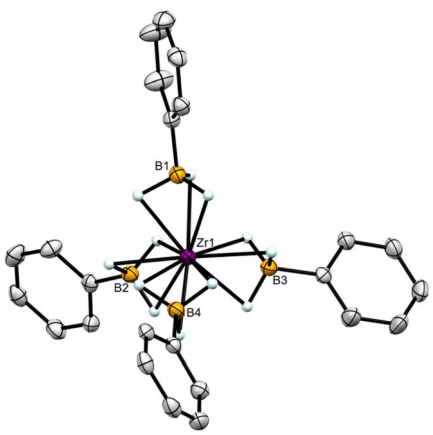


Fig. 2 Molecular structure of $[Zr(PhBH_3)_4]$. Ellipsoids are drawn at the 35% probability level. Hydrogen atoms on carbon are omitted from the figure.


© 2025 The Author(s). Published by the Royal Society of Chemistry

Open Access Article. Published on 29 October 2025. Downloaded on 2/23/2026 2:13:50 AM. This article is licensed under a Creative Commons Attribution-NonCommercial 3.0 Unported Licence.

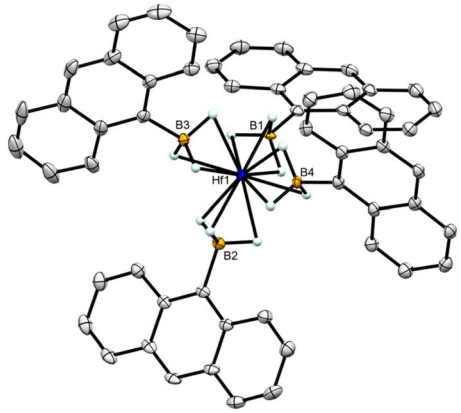


Fig. 3 Molecular structure of [Hf(AnthBH$_3$)$_4$]. Ellipsoids are drawn at the 35% probability level. Hydrogen atoms on carbon and co-crystallized toluene are omitted from the figure.

toluene solutions with pentane. The complexes did not exhibit any appreciable volatility when sublimation was attempted up to 100 °C at $10^{-2}$ torr. Related group 4 complexes were not pursued with titanium because $Ti^{4+}$ is known to be unstable with respect to reduction to $Ti^{3+}$ in the presence of borohydride ligands.[39,40]

Single-crystal X-ray diffraction (XRD) studies revealed the expected tetrahedral coordination geometries based on the arrangement of the boron atoms around the metal (representative structures shown in Fig. 2 and 3). Metal–ligand bond distances from XRD are often used as a first assessment of bonding and electronic structure changes in coordination complexes, but this can be a challenge with borohydride ligands. As is the case here, hydrides can sometimes be observed in XRD difference maps, but the positions usually suffer from high uncertainties due to the low X-ray scattering cross-section of hydrogen. Other techniques like neutron diffraction are often required to identify hydrogen positions, but even this can be challenging for borohydride complexes given the high neutron absorption cross-section of $^{10}$B in naturally occurring boron.[41] These challenges highlight the need for developing new spectroscopic approaches like B K-edge XAS to interrogate metal–borohydride bonding. This is also why M−B distances obtained from XRD continue to be the most useful structural assessment of bonding differences in metal borohydride complexes.

The M–B bond distances and modeled hydrogen positions (fixed with B–H = 1.20 Å; see experimental details) were consistent with the expected 12-coordinate structures with tridentate-bound ligands. The average M−B distances of [Zr(PhBH$_3$)$_4$] and [Hf(PhBH$_3$)$_4$] were 2.325(5) Å and 2.295(7) Å, respectively (Table 1), similar to other Zr and Hf complexes with $\kappa^3$ trihydroborates.[42–44] For comparison, Zr–B distances in [Cp$_2$Zr(PhBH$_3$)$_2$] with equivalent $\kappa^2$-bound PhBH$_3^{1-}$ were significantly longer at 2.628(6) Å.[45] To quantify the coordination geometry of these complexes, the four-coordinate geometry index ($\tau_4$) was employed.[46] The $\tau_4$ values for all the structures ranged from 0.96 to 0.99, indicating only small deviations from rigorously tetrahedral coordination geometry ($\tau_4 = 1$) based on boron positioning.

$^1$H and $^{11}$B NMR data collected for the [M(RBH$_3$)$_4$] complexes in C$_6$D$_6$ corroborated the formulations and revealed differences in chemical shifts that can be attributed to metal and boron substituent identity (Table 1). The $^1$H NMR resonances assigned to the BH$_3$ groups appear as a broad feature in each spectrum with shifts ranging from $\delta_H$ 1.7 ppm for [Zr(BnBH$_3$)$_4$] to $\delta_H$ 4.9 ppm for [Hf(AnthBH$_3$)$_4$]. The $^{11}$B NMR spectra similarly revealed a single broad resonance with shifts ranging from $\delta_B$ −4.2 ppm for [Hf(PhBH$_3$)$_4$] to $\delta_B$ −0.4 ppm for [Zr(BnBH$_3$)$_4$] and [Zr(AnthBH$_3$)$_4$].

Plotting the BH$_3$ chemical shifts for the [Zr(RBH$_3$)$_4$] complexes with R = aryl revealed a clear stepwise shift downfield for both the $^1$H and $^{11}$B resonances in accordance with the increasing sterics of Ph to Mes to Trip to Anth (Fig. 4a). The BH$_3$ resonances for the [Hf(RBH$_3$)$_4$] complexes with the same aryl substituents show an identical trend, albeit with points shifted down and to the right on the plot due to the change in metal identity. The $^1$H NMR resonances for the [Hf(RBH$_3$)$_4$] complexes are shifted more downfield compared to their Zr analogs, whereas the $^{11}$B NMR resonances are shifted more upfield.

Table 1 Spectroscopic data for BH$_3$ groups (NMR and IR) and M−B distances and $\tau_4$ values from single-crystal XRD studies. NMR data were obtained in C$_6$D$_6$ at 20 °C. The identity of the [M(RBH$_3$)$_4$] complexes are abbreviated as M–R where M = metal and R = substituent attached to boron

| Complex | $^1$H shift (ppm) | $^{11}$B shift (ppm) | B–H stretch (cm$^{-1}$) | Avg. M−B distance (Å)[a] | $\tau_4$[46] |
|---|---|---|---|---|---|
| Zr-Ph | 2.8 | −2.1 | 2134, 2075 | 2.325(5) | 0.99 |
| Hf-Ph | 3.5 | −4.2 | 2146, 2086 | 2.295(7) | 0.98 |
| Zr-Bn | 1.7 | −0.4 | 2129, 2077 | 2.327(3) | 0.99 |
| Hf-Bn | 2.4 | −3.7 | 2136, 2087 | 2.309(7) | 0.99 |
| Zr-Mes | 2.9 | −1.6 | 2145, 2036 | [b] | * |
| Hf-Mes | 3.7 | −3.7 | 2143, 2055 | [b] | * |
| Zr-Trip | 3.4 | −0.8 | 2144, 2034 | [b] | * |
| Hf-Trip | 4.2 | −3.3 | 2153, 2044 | 2.313(8) | 0.97 |
| Zr-Anth | 4.1 | −0.4 | 2150, 2092 | 2.328(11) | 0.96 |
| Hf-Anth | 4.9 | −2.9 | 2168, 2090 | 2.311(9) | 0.98 |

[a] ESD's denote the standard deviation of the averaged M−B distances. [b] Crystals obtained were not of sufficient quality for XRD analysis.

Open Access Article. Published on 29 October 2025. Downloaded on 2/23/2026 2:13:50 AM.
This article is licensed under a Creative Commons Attribution-NonCommercial 3.0 Unported Licence.

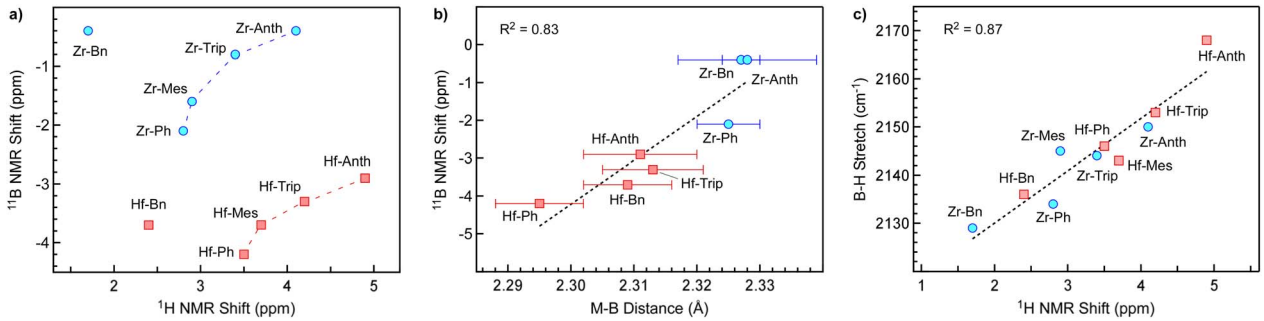


Fig. 4 Spectroscopic comparisons for $[M(RBH_3)_4]$ complexes with M = Zr (blue circles) or Hf (red squares). (a) Comparison of $^{1}$H and $^{11}$B NMR shifts assigned to $BH_3$ resonances in $C_6D_6$ at RT. The dashed lines are shown to emphasize the trends between the data points for complexes with different aryl substituents. (b) Comparison of $^{11}$B NMR shifts to M–B distances from single-crystal XRD studies. Error bars denote the standard deviation of the average M–B distances. (c) Comparison of the higher energy B–H stretches obtained from the IR spectra to $^{1}$H NMR shifts for the $BH_3$ resonances. The black dashed line in panels (b) and (c) is the linear fit to all data points shown.

Perhaps unsurprisingly, the chemical shifts for the complexes with R = benzyl (an alkyl) deviate significantly from those with R = aryl, but the influence of metal identity is maintained with the data point for $[Hf(BnBH_3)_4]$ again trending down and to the right in the plot relative to $[Zr(BnBH_3)_4]$. Incidentally, these metal dependent trends in the $^{1}$H and $^{11}$B NMR data follow those reported for $[Zr(BH_4)_4]$ ($\delta_H = 1.5$ ppm; $\delta_B = -8.2$ ppm) and $[Hf(BH_4)_4]$ ($\delta_H = 2.7$ ppm; $\delta_B = -11.3$ ppm).[47]

Given the apparent steric influence of the R substituents on the NMR data, we postulated that the $^{11}$B NMR shifts would likely correlate to structural data obtained from the single-crystal XRD studies. Indeed, plots of the $^{11}$B NMR shifts to average M–B distances reveal a good correlation with $R^2 = 0.83$ (Fig. 4b). Unfortunately, a similar comparison could not be made with the hydrides due to the above-mentioned challenges effectively modeling hydrogen positions using single-crystal XRD. The average M–H distances for all the complexes were effectively identical at 2.2(1) Å after accounting for the relatively high standard deviation and uncertainties. However, we reasoned that the $^{1}$H NMR data may correlate to another hydride reporter, namely B–H stretches obtained from IR spectra. The IR spectra of the Zr and Hf complexes yield two absorptions assigned to B–H stretching around 2100 cm$^{-1}$ (Table 1). In the $T_d$ point group, these would be assigned as IR-allowed absorptions of $T_2$ symmetry,[48–50] but the point group symmetry is lower and better approximated as $S_4$ (see group theory analysis below). Collectively, the IR absorptions are consistent with the bridging B–H stretching modes and $\kappa^3$ coordination of the trihydroborate ligands. For comparison, the B–H stretching frequencies reported previously for $[Zr(MeBH_3)_4]$ were 2140 and 2080 cm$^{-1}$.[42]

The higher energy B–H stretches from the IR spectra show subtle metal and substituent-dependent differences that correlate well when plotted against the $^{1}$H NMR shifts ($R^2$ = 0.87; Fig. 4c). Interestingly, the lower energy B–H stretching absorptions showed no correlation when plotted the same way, but there may be additional underlying vibrational modes or overtones contributing to these absorptions. In this context, we note that some of these IR features exhibited shoulders and were less resolved than others.

The correlation between B–H stretches and the $^{1}$H NMR shifts for the $BH_3$ groups is perhaps unsurprising given that both spectroscopic techniques are known to be influenced by changes in metal–ligand covalency. It is well understood that ligand bonds such as B–H weaken and vibrate at lower frequencies when they donate electron density to metals. It is also known that NMR chemical shifts are sensitive to changes in metal–ligand covalency.[51] The correlation in Fig. 4c suggests that upfield $^{1}$H shifts like that observed for $[Zr(BnBH_3)_4]$ are indicative of increased covalent M–H–B bonds and downfield shifts correspond to those that are less covalent. If true, these data would suggest that Zr–H–B bonds are generally more covalent than those with Hf when the identity of the substituent attached to boron is the same. Interestingly, this assessment is consistent with prior quasi-relativistic Xα-SW calculations comparing $[Zr(BH_4)_4]$ and $[Hf(BH_4)_4]$, which suggested that metal–ligand bonding is more ionic in the Hf complex.[52]

## B K-edge XAS studies

B K-edge XAS experiments were conducted on the Zr and Hf complexes, as well as some of their lithium salts, to investigate the presence of covalent M–H–B bonding. The XAS experiments were performed at the Canadian Light Source using the Variable Line Spacing Plane Grating Monochromator (VLS-PGM) beamline.[53]

Given the notoriously high air and water sensitivity of transition metal borohydride complexes, initial efforts were aimed at optimizing the sample preparation and loading to ensure that sample hydrolysis was minimized. XAS samples of the borohydride complexes were prepared in an Ar-filled glovebox using equipment dried in a muffle furnace at 150 °C (see experimental section) and loaded using an Ar purge box attached to the sample chamber. Upon loading, the samples were immediately evacuated to ~$10^{-6}$ torr before being transported under vacuum using actuating arms to the main sample chamber for measurement at $10^{-8}$–$10^{-10}$ torr. Features assigned to hydrolysis were determined by measuring samples that were allowed to sit in air for 20–30 min. The hydrolyzed samples revealed no B K-edge transitions below 192 eV where


© 2025 The Author(s). Published by the Royal Society of Chemistry

Open Access Article. Published on 29 October 2025. Downloaded on 2/23/2026 2:13:50 AM. This article is licensed under a Creative Commons Attribution-NonCommercial 3.0 Unported Licence.

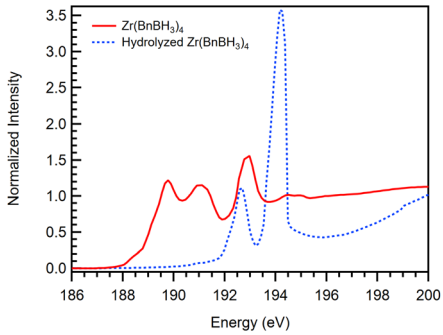


Fig. 5 Representative comparison of the B K-edge XAS spectra for a sample of $[Zr(BnBH_3)_4]$ before (solid red) and after (dashed blue) exposure to air.

pre-edge features associated with M–H–B bonding are observed (Fig. 5). The hydrolyzed samples instead revealed two prominent features at higher energy consistent with B–O bond containing species.[54–56]

Aside from hydrolysis, another challenge that became apparent in our initial data collection efforts was beam-induced photodecomposition. This was evident with visual charring of the sample even after relatively short scans, though changes in the spectra due to photodecomposition were relatively subtle and too fast to be observed unless beam exposure was limited when collecting data on the same spot. Similar issues associated with photo-induced decomposition features were also observed by us previously for B K-edge XAS spectra collected on the bis(dicarbollide) complex $[Ni(C_2B_9H_{11})_2]$.[32]

To characterize the ingrowth of photodecomposition features, multiple scans were collected for each complex at the same sample position. A representative example of these spectra is shown in Fig. 6 for $[Hf(AnthBH_3)_4]$, and spectra for all the complexes investigated are provided in the SI. The first scan collected on $[Hf(AnthBH_3)_4]$ (depicted in red in Fig. 6) revealed a broad pre-edge feature centered at 190.3 eV and two higher energy features at 192.3 and 193.9 eV. After the first scan on $[Hf(AnthBH_3)_4]$, the intensity of the broad feature at 190.3 eV begins to decrease stepwise and a new feature grows in at 189.3 eV, as determined by analysis of the second derivative traces (see the SI). The identity of the decomposition products

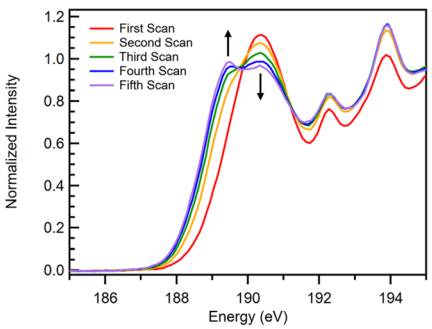


Fig. 6 B K-edge XAS spectrum of $[Hf(AnthBH_3)_4]$ as more fast scan measurements are collected on a single sample spot.

are unknown, but we note that the energies of these features are similar to where absorptions have been observed in B K-edge XAS studies of $ZrB_2$, which appear at around 188 eV.[57] The two features beyond 192 eV could be associated with small amounts of hydrolysis, which may account for why they appear relatively unchanged from scan to scan. However, as we will show below in the following sections, simulated spectra from TDDFT calculations suggest features in this higher energy region, indicating that they could be associated with the sample.

Collectively, our hydrolysis and photodecomposition studies illustrate the significant challenges collecting B K-edge XAS data on homoleptic borohydride complexes. It is difficult to eliminate these contributions completely from the spectra for all the complexes described here given the facilities currently available. Spectra collected on the benzyl-substituted complexes were too reactive to obtain reproducible data when moving between different sample positions. The spectrum of $[Zr(BnBH_3)_4]$ provided in Fig. 5, for example, reveals significant photodecomposition even after the first scan. Similar problems were encountered for the $(TripBH_3)^{1-}$ complexes. In a related observation, it appears that the Zr complexes undergo photodecomposition faster than the Hf complexes, which is evident in the Zr and Hf spectral comparisons shown in Fig. 7. Despite these inherent challenges, reproducible spectra were successfully collected on the phenyl, mesityl, and anthryl-substituted

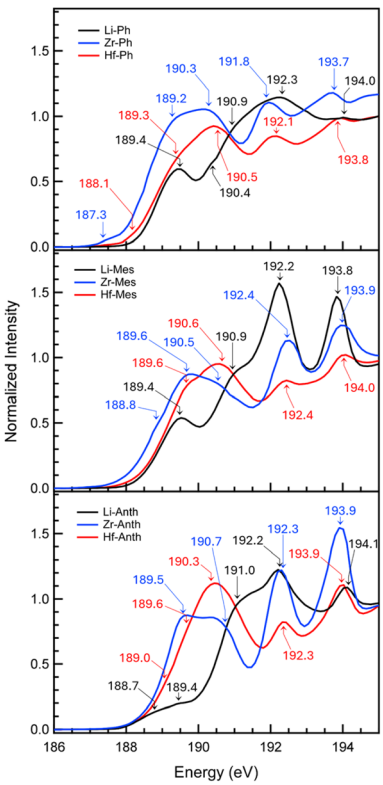


Fig. 7 B K-edge XAS spectra of $[M(RBH_3)_4]$ complexes with M = Zr (blue) and Hf (red) and comparison to their corresponding $Li(RBH_3)$ salts (black). Labeled positions indicate peak maxima in the spectra or peak positions identified by analysis of the second derivate traces (Fig. S51–S53; SI).

Open Access Article. Published on 29 October 2025. Downloaded on 2/23/2026 2:13:50 AM. This article is licensed under a Creative Commons Attribution-NonCommercial 3.0 Unported Licence.

borohydride complexes. Some photodecomposition is still observed despite minimizing beam exposure and moving the sample position after each scan, but the data clearly reveal spectral features that can be attributed to covalent three-center, two-electron M–H–B bonding.

B K-edge XAS data collected on the $[M(RBH_3)_4]$ complexes with M = Zr and Hf, as well as their $Li(RBH_3)$ salts with R = Ph, Mes, Anth are provided in Fig. 7. Beginning with the phenyltrihydroborate complexes, the spectra of $[Zr(PhBH_3)_4]$ and $[Hf(PhBH_3)_4]$ each revealed a broad pre-edge feature defined by two minima in the second derivative traces. The peak positions were located at 189.2 and 190.3 eV for M = Zr, and these were shifted to slightly higher energy at 189.3 and 190.5 eV for M = Hf. Both spectra revealed two higher energy absorptions on top of the rising edge around 192 and 194 eV. For comparison, the spectrum for $Li(PhBH_3)$ revealed a single pre-edge feature at 189.4 eV followed by a broad and relatively unresolved rising edge feature. We note that peak intensities vary, but the relatively short post-edge (which was truncated to help minimize photodecomposition) does not allow for normalization of the spectra at the level required for careful intensity comparisons.

The spectra for the Li, Zr, and Hf complexes with R = Mes and Anth are similar to those for R = Ph, albeit with subtle differences in the peak positions (Fig. 7). In general, the pre-edge features for the Hf complexes are blue shifted compared to the those with Zr. As observed previously,[58–61] this is attributed to orbital mixing with the higher energy 5d orbitals of Hf as compared to 4d orbitals with Zr. However, we note that the position of the first pre-edge feature in most of the spectra appears close to the same position for the features attributed to photodecomposition. Density functional theory (DFT) and time-dependent density functional theory (TDDFT) calculations were therefore carried out to help delineate between features associated with the complexes and those attributed to decomposition. To help guide the discussion of the DFT results, it is instructive to first introduce the relevant frontier orbitals responsible for metal–ligand bonding using group theory.

## Group theory analysis

We have selected $(PhBH_3)^{1-}$ and $[Zr(PhBH_3)_4]$ as examples for the following analysis, but the results from this approach are generally representative of all the ligands and complexes described in this study given their similar structures and point group symmetries. Like the other trihydroborate anions, $(PhBH_3)^{1-}$ possesses $C_s$ point group symmetry, which can be attributed to the phenyl substituent eliminating the $C_3$ axis more commonly encountered in traditional borohydrides like $(BH_4)^{1-}$ and $(MeBH_3)^{1-}$. A notable consequence of $C_s$ symmetry is that it dictates the coordinate system for $(PhBH_3)^{1-}$ and orients the $z$-axis perpendicular to the $\sigma_h$ mirror plane, as shown in Fig. 8a.

With regards to the MOs expected for $(PhBH_3)^{1-}$, we will limit our discussion to the occupied and donor-capable orbitals containing boron and hydrogen. In $C_s$ symmetry, there are three occupied MOs of B 2p parentage that can be assigned as a′, a′, and a″ (total: 2a′ + a″; Fig. 8a). The a′ MO assigned as B–C $\sigma$ involves mixing between the B $2p_x$ and C 2p orbital on the attached phenyl substituent. As our DFT calculations will show, this MO lacks significant electron density on the hydrogen atoms and is thus relatively non-bonding when combined with metals. In contrast, the remaining a′ and a″ MOs have significant electron density located on the hydrogen atoms. These MOs are best described as B–H $\sigma$, and they arise from the B $2p_z$ and B $2p_y$ orbitals mixing with the symmetry adapted linear combinations (SALCs) of H 1s orbitals of corresponding symmetry (Fig. 8a). Consistent with the increased electron density at hydrogen, the two B–H $\sigma$ MOs are those primarily responsible for M–H–B bonding with Zr and Hf.

We next consider the point group symmetry of $[Zr(PhBH_3)_4]$ and the corresponding arrangement of $(PhBH_3)^{1-}$ ligands

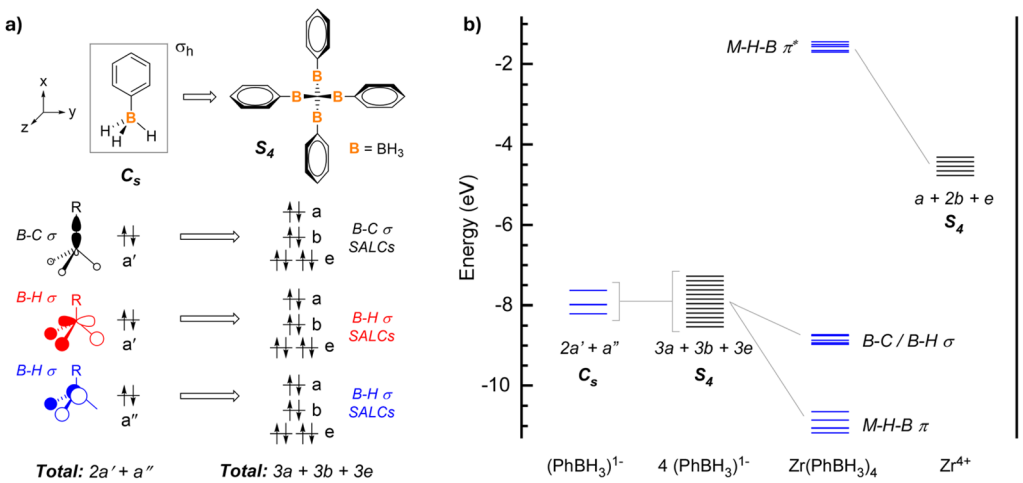


Fig. 8 (a) Occupied $(PhBH_3)^{1-}$ MOs in $C_s$ point group symmetry containing B 2p character and the corresponding SALCs derived from four $(PhBH_3)^{1-}$ arranged as shown with $S_4$ point group symmetry. The coefficients indicate the total number of each Mulliken symbol. (b) MO correlation diagram for $[Zr(PhBH_3)_4]$ in $S_4$ point group symmetry starting from occupied $(PhBH_3)^{1-}$ MOs depicted in part a. The MO energies shown in blue were obtained from DFT calculations for $Li(PhBH_3)$ and $[Zr(PhBH_3)_4]$. The energies of the twelve $(PhBH_3)^{1-}$ SALCs and $Zr^{4+}$ 4d orbitals in black are approximated.


© 2025 The Author(s). Published by the Royal Society of Chemistry

Open Access Article. Published on 29 October 2025. Downloaded on 2/23/2026 2:13:50 AM. This article is licensed under a Creative Commons Attribution-NonCommercial 3.0 Unported Licence.

around the metal. The point group of $[Zr(PhBH_3)_4]$ is relatively low when considering the experimental and DFT-optimized structures, but it can be approximated as $S_4$ based on the canted arrangement of the phenyl substituents (Fig. 8a). Expanding the three occupied MOs identified for $(PhBH_3)^{1-}$ in $C_s$ symmetry to an $S_4$ arrangement of four ligands yields 12 SALCs that reduce to 3a + 3b + 3e (coefficients indicate the total number of each Mulliken symbol). These SALCs are of appropriate symmetry to mix with the five Zr 4d orbitals, which have Mulliken symbols of a ($d_{z^2}$), b ($d_{x^2-y^2}$ and $d_{xy}$), and e (degenerate $d_{xz}$ and $d_{yz}$) in $S_4$ symmetry. Five bonding and antibonding combinations are expected to arise due to M–H–B orbital mixing. The remaining SALCs, particularly those that derive from B–C $\sigma$ MOs on the ligand, are expected to be relatively non-bonding with respect to the metal. Collectively, the resulting MOs from group theory yield the MO diagram shown in Fig. 8b, which indeed matches that obtained from the DFT calculations described in the following section.

Table 2 Energy and composition of calculated M–H–B π* MOs for $[Zr(PhBH_3)_4]$ and $[Hf(PhBH_3)_4]$.[a]

| | Assignment[b] | Energy (eV) | Metal *n*d | Metal *n*p | B 2p | H 1 s |
|---|---|---|---|---|---|---|
| $[Zr(PhBH_3)_4]$ | 2b ($d_{xy}$) | −1.44 | 66% | 2% | 17% | 10% |
| | 1e ($d_{xz}$) | −1.51 | 53% | 3% | 19% | 10% |
| | 1a ($d_{z^2}$) | −1.56 | 63% | 1% | 15% | 7% |
| | 1e ($d_{yz}$) | −1.66 | 53% | 2% | 18% | 9% |
| | 1b ($d_{x^2-y^2}$) | −1.70 | 54% | 1% | 17% | 7% |
| $[Hf(PhBH_3)_4]$ | 2b ($d_{xy}$) | −0.73 | 62% | 3% | 19% | 9% |
| | 1a ($d_{z^2}$) | −0.84 | 56% | 1% | 14% | 5% |
| | 1e ($d_{xz}$) | −1.06 | 39% | 5% | 21% | 8% |
| | 1b ($d_{x^2-y^2}$) | −1.14 | 41% | 3% | 18% | 6% |
| | 1e ($d_{yz}$) | −1.21 | 36% | 4% | 21% | 8% |

[a] Energies and composition for the M–H–B π MOs and relevant MOs for the other complexes can be found in the SI. [b] MO assignments were made assuming $S_4$ point group symmetry.

## DFT calculations

Ground state density functional theory (DFT) calculations were performed to quantify the energies and compositions of MOs derived from group theory. The calculations were performed using dispersion-corrected B3LYP[62,63] with LANL08(f)[64–66] and double-z 6-31G(d,p)[67] basis sets because we have shown that this level of theory performs consistently well for modeling ligand K-edge XAS spectra using time-dependent density functional theory (TDDFT).[68–79] The calculated bond distances and angles were in good agreement with the experimental data obtained by single-crystal XRD (Table S2; SI). The DFT optimized structures allowed analysis of the hydride distances and angles, which were less reliable from single-crystal XRD analysis due to the low scattering cross-section of hydrogen. The average B–H distances for each complex from theory were identical within error, ranging from 1.247(8)–1.253(7) Å. The average M−H distances were also similar for each metal with the Zr complexes ranging from 2.10(2)–2.12(3) Å and the Hf complexes being slightly shorter at 2.08(7)–2.09(2) Å due to the smaller radius of Hf ($Zr^{4+}$ = 0.59 Å and $Hf^{4+}$ 0.58 Å; CN = 4).[80]

The DFT-optimized structures revealed Zr and Hf complexes with distorted tetrahedral coordination geometries and approximate $S_4$ point group symmetry consistent with our experimental results. The DFT calculations confirmed the presence of the MOs predicted for $[Zr(PhBH_3)_4]$ using group theory and yielded their energies, which are shown in Fig. 8b and compiled in Table 2. Analysis of the Kohn–Sham orbitals revealed that the metal–ligand bonding and antibonding orbitals are M–H–B π and π*, respectively (Fig. 9). These orbitals are typically referred to as π bonding interactions based on the relative arrangement of the B 2p and metal d-orbitals.[9,10] The Kohn–Sham plots and orbital analysis do not yield significant evidence of direct M−B $\sigma$* bonding, which has been invoked previously for complexes such as $[Hf(BH_4)_4]$.[49]

All five M–H–B π* MOs have relatively consistent Zr 4d (53–66%), B 2p (15–19%), and H 1s character (7–10%) and comparable energies, as shown in Table 2 and Fig. 9. The window

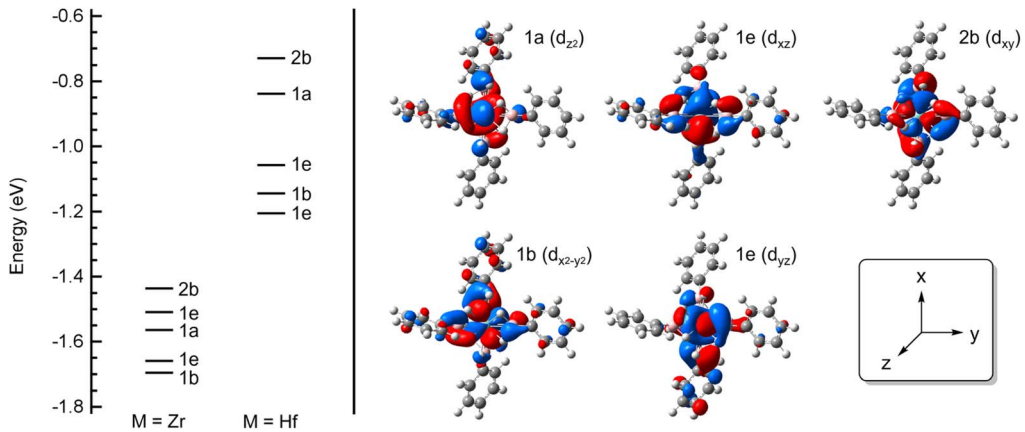


Fig. 9 Left – quantitative ligand field splitting diagram for $[Zr(PhBH_3)_4]$ and $[Hf(PhBH_3)_4]$ using MO energies from the DFT calculations. The Mulliken symbols provided are used to assign MOs and associated d-orbitals in idealized $S_4$ symmetry, but the actual symmetry is lower and breaks the degeneracy of those assigned as 1e. Right – Kohn–Sham plots of the first five unoccupied MOs calculated for $[Zr(PhBH_3)_4]$ with their corresponding d-orbital parentage and MO labels. MOs were plotted using GuassView 5 (ref. 81) with an iso value of 0.03.

Open Access Article. Published on 29 October 2025. Downloaded on 2/23/2026 2:13:50 AM. This article is licensed under a Creative Commons Attribution-NonCommercial 3.0 Unported Licence.

containing all five MOs is 0.26 eV (2100 $cm^{-1}$). A similar picture emerges when evaluating the compositions of the bonding MOs. The M–H–B π orbitals have higher B 2p (18–24%) and H 1s (32–43%) character and lower Zr 4d (9–16%) (Table S5; SI), as expected given that the MOs are derived from the $(PhBH_3)^{1-}$ ligand SALCs. These results suggest that all five d-orbitals participate rather evenly in metal–borohydride bonding.

Consistent with the inherent energy differences between 4d and 5d orbitals, the five unoccupied M–H–B π* MOs for $[Hf(PhBH_3)_4]$ shift to higher energy as compared to those for $[Zr(PhBH_3)_4]$. The ordering of the MOs also changes slightly and the manifold of energies widens, which is attributed to the Hf 5d-character decreasing in the first three MOs (36–41%), as compared to the 4d-character in the same MOs for $[Zr(PhBH_3)_4]$ (53–63%). In contrast to the change in metal d-character, the M–H–B π* MOs for $[Hf(PhBH_3)_4]$ maintain percentages of B 2p and H 1s character similar to those calculated for $[Zr(PhBH_3)_4]$ (Table 2). The decrease in M–H–B orbital mixing for Hf as compared to Zr in the same MOs suggests that the M–H–B bonding is less covalent in $[Hf(PhBH_3)_4]$. This appears to be consistent with NMR and IR comparisons presented in Fig. 4 that imply that Zr–H–B bonds are more covalent than those with Hf when the identity of the substituent attached to boron is the same.

The calculated MO compositions and energies for $[Zr(MesBH_3)_4]$ and $[Hf(MesBH_3)_4]$ follow the same general trends as those observed for the phenyltrihydroborate complexes (Table S6). Similar trends are also observed for $[Zr(AnthBH_3)_4]$ and $[Hf(AnthBH_3)_4]$, but the MOs of metal parentage are significantly more delocalized due to the larger manifold of π-based orbitals associated with the anthracenyl backbone. The calculations revealed that the first four unoccupied orbitals for $[Hf(AnthBH_3)_4]$ are primarily π-based orbitals localized on the ligand. The LUMO for $[Hf(AnthBH_3)_4]$, for example, is comprised of only 8.0% Hf 5d and 5.9% B 2p character. The primary MOs of 5d parentage begin at LUMO + 4 (Table S7; SI). The increased number of unoccupied MOs containing B 2p character for $[Zr(AnthBH_3)_4]$ and $[Hf(AnthBH_3)_4]$ is expected to give rise to a larger manifold of B K-edge XAS transitions, which is indeed observed in simulated spectra described in the following section.

### TDDFT calculations

TDDFT calculations were performed to simulate the B K-edge XAS spectra and provide spectral assignments. Plots comparing the $[M(RBH_3)_4]$ complexes with different metals and the same R substituents (R = Ph with M = Zr and Hf) and the same metal with different R substituents (M = Hf with R = Ph, Mes, Anth) are shown in Fig. 10 (TDDFT comparisons for the other complexes can be found in the SI). Along with the Zr and Hf borohydride complexes, we also performed TDDFT calculations for $Li(PhBH_3)$ and $Li(AnthBH_3)$ to confirm the pre-edge features observed in the ligand salt precursors were different than those observed for the metal complexes (Fig. S54; SI).

In general, the simulated spectra reproduce the most salient features of the experimental spectra aside from the first pre-edge shoulder where photodecomposition features were noted to appear (see above). The simulated spectra for the Zr and Hf complexes confirm that the first feature is not associated with the complexes and can indeed be attributed to photodecomposition. The TDDFT calculations indicate three dominant bands of transitions. The first cluster of transitions calculated for $[Zr(PhBH_3)_4]$ are assigned as B 1s → Zr–H–B π*, and these involve the first five unoccupied MOs shown in Fig. 8 and 9. The higher-energy features above the rising edge are assigned to ligand-based transitions associated with B-aryl bonds and Rydberg states. Consistent with their assignment, the energy of these higher energy features is similar for $[Zr(PhBH_3)_4]$ and $[Hf(PhBH_3)_4]$. By contrast, the first feature assigned as B 1s → M–H–B π* transitions for M = Zr shifts to higher energy for M = Hf, as expected based on the increased energy of the Hf–H–B π* MOs (Fig. 9). The blue shift observed for the B 1s → Hf–H–B π* transitions is wholly attributed to the differences in the energy of the M–H–B π* MOs; the calculated energies of the B 1s

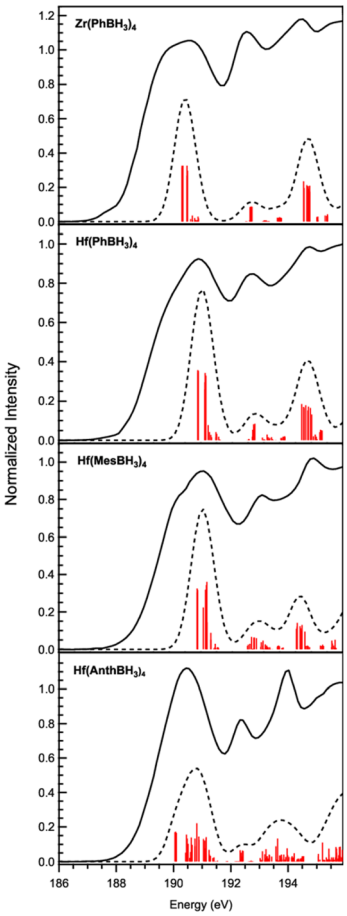


Fig. 10 Comparison of experimental and simulated B K-edge XAS data. The experimental spectra (solid lines), simulated spectra (dashed lines), and calculated transitions (red bars) are shown. Calculated oscillator strengths were multiplied by a factor of 22 to bring them on scale with the experimental data. An energy shift of +9.6 eV was applied to the calculated spectra so that relative differences in calculated and experimental peak positions could be compared. The simulated spectra were obtained by applying a Gaussian broadening with FWHM = 0.45 to the individual transitions.


© 2025 The Author(s). Published by the Royal Society of Chemistry

Open Access Article. Published on 29 October 2025. Downloaded on 2/23/2026 2:13:50 AM. This article is licensed under a Creative Commons Attribution-NonCommercial 3.0 Unported Licence.

orbitals (where the promoted electrons originate) are nearly identical for $[Zr(PhBH_3)_4]$ and $[Hf(PhBH_3)_4]$ (Table S5; SI).

The simulated spectra and transitions for the R = Mes complexes are similar to those for the R = Ph complexes but differ significantly for R = Anth. We provide the comparisons of $[Hf(PhBH_3)_4]$, $[Hf(MesBH_3)_4]$, and $[Hf(AnthBH_3)_4]$ in Fig. 10 to show how the differing aryl substituents with the same metal influence the simulated spectra (plots for the Zr complexes with R = Mes and Anth are provided in Fig. S55; SI). The increased conjugation of the anthracenyl backbone and more diffuse aryl $\pi$ orbitals lead to more unoccupied B 2p orbitals available for transitions and a broader pre-edge feature. The pre-edge feature includes B 1s $\rightarrow$ Hf–H–B $\pi^*$ transitions, but also ligand-centered B 1s $\rightarrow$ B–C $\pi^*$ transitions that mix into the 5d manifold. This makes it difficult to tease out how the calculated spectral intensities correlate to suspected substituent-dependent differences in M–H–B covalency.

# Conclusion

We have described what appears to be the first B K-edge XAS and TDDFT study of homoleptic transition metal borohydride complexes. To facilitate the required measurements in ultra-high vacuum, a series of relatively non-volatile $[Zr(RBH_3)_4]$ and $[Hf(RBH_3)_4]$ complexes were prepared with different alkyl and aryl groups attached to boron (R = Bn, Ph, Mes, Trip, and Anth). The complexes were characterized by NMR and IR spectroscopy and single-crystal XRD, and the data revealed spectral and structural correlations suggestive of metal- and substituent-dependent differences in metal–borohydride bonding.

B K-edge XAS spectra collected on the Zr and Hf complexes with R = Ph, Mes, and Anth revealed absorption features indicative of covalent M–H–B bonding. These features could be clearly discerned from those attributed to photodecomposition, and they were assigned as B 1s $\rightarrow$ M–H–B $\pi^*$ based on group theory analysis and comparison to supporting (TD)DFT calculations. The presence of photodecomposition did not permit rigorously quantitative intensity comparisons, as needed to assess the suspected influence of metal and substituent identity on metal–borohydride covalency. However, the pre-edge features revealed the expected shift to higher energy from Zr to Hf consistent with the change in 4d and 5d orbital energies.[58–61] This study shows that even though boron is not directly bound to the metal, the delocalized nature of three-center, two-electron bonds yields significant M–H–B orbital mixing that can be identified spectroscopically using boron as a reporter. Moreover, these results establish how ligand K-edge XAS may be used more generally to measure covalent three-center, two-electron bonding in other complexes.

# Experimental

### General considerations

All reactions were carried out under an atmosphere of Ar or $N_2$ using glovebox or standard Schlenk techniques. All glassware was heated at 150 °C for at least 2 h and allowed to cool under vacuum before use. Solvents were dried and deoxygenated using a Pure Process Technologies Solvent Purification System and stored over 3 Å molecular sieves. Deuterated solvents were deoxygenated with three freeze–pump–thaw cycles and stored over 3 Å molecular sieves. The lithium borohydride salts $Li(PhBH_3)$,[33] $Li(MesBH_3)$,[34] $Li(TripBH_3)$,[35] $Li(AnthBH_3)$,[36] and $Li/K(BnBH_3)$[37] were prepared as described previously. Their formulations were verified by NMR spectroscopy before use, and representative spectra are shown for $Li(MesBH_3)$ in the SI. The salts were isolated from $Et_2O$ or thf solutions and stored under dynamic vacuum for at least several hours before use. The salts retain small amounts of the corresponding ether used in their preparation, but stoichiometry calculations used for the following reactions assume that the amount is negligible. Anhydrous $ZrCl_4$ and $HfCl_4$ were purchased from Strem Chemicals and used as received.

$^1H$ NMR data were collected on a Brucker Avance-300 spectrometer at 300 MHz, a Bruker Avance-400 operating at 400 MHz, or a Bruker Avance-500 operating at 500 MHz. $^{11}B$ NMR data were collected on a Brucker Avance-300 spectrometer at 96 MHz, a Bruker Avance-400 operating at 128 MHz, or a Bruker Avance-500 operating at 160 MHz. Chemical shifts are reported in $\delta$ units relative to residual NMR solvent peaks ($^1H$) and $BF_3 \cdot Et_2O$ ($^{11}B$ $\delta$ 0.0 ppm). IR spectra were acquired with a Thermo Scientific Nicolet iS5 in an $N_2$-filled glovebox as KBr pellets, Nujol mulls, or using an attenuated total reflectance (ATR) accessory equipped with a diamond crystal. Elemental analysis data (C, H, N) were collected on an Exeter Analytical CE-440 elemental analyzer at the University of Iowa MATFab facility. The data were consistently low in carbon and hydrogen, likely due to incomplete combustion and/or metal carbide formation. Similarly low carbon and hydrogen values were reported for Th and U complexes containing some of the same borohydride ligands reported here.[82] The elemental analysis data that were collected are provided for transparency.

### Tetrakis(phenyltrihydroborato)zirconium(IV), $[Zr(PhBH_3)_4]$

$ZrCl_4$ (0.200 g, 0.862 mmol) and $Li(PhBH_3)$ (0.336 g, 3.43 mmol) were stirred overnight in pentane (10 mL). The solution was filtered through a pad of Celite, and the filtrate was evaporated to dryness under vacuum. The light brown solid was dissolved in the minimum amount of pentane and placed in a freezer at −30 °C. Light brown needle-like crystals formed overnight. Yield: 214 mg (55%). M.p.: 130 °C (dec). Anal. calcd for $C_{24}H_{32}B_4Zr$: C, 63.36; H, 7.09. Found (run 1): C, 53.70; H, 5.38. Found (run 2): C, 53.64; H, 5.38. Found (run 3): C, 51.42; H, 5.00. $^1H$ NMR (500 MHz, $C_6D_6$, $\delta$): 7.70–7.65 (m, 4H, CH), 7.43–7.19 (m, 16H, CH), 2.78 (br s, 12H, $BH_3$). $^{11}B$ NMR (128 MHz, $C_6D_6$, $\delta$): −2.1 (br s, $BH_3$). IR (KBr) $\bar{\nu}_{max}$ ($cm^{-1}$) 3070 (m), 3050 (m), 3016 (m), 2965 (m), 2137 (s), 2075 (s), 1601 (s), 1493 (w), 1434 (s), 1336 (s), 1302 (s), 1265 (s), 1240 (s), 1159 (m), 1099 (m), 1025 (s), 909 (w), 884 (w), 808 (s), 740 (s), 696 (s).

### Tetrakis(phenyltrihydroborato)hafnium(IV), $[Hf(PhBH_3)_4]$

Prepared as described for $[Zr(PhBH_3)_4]$ with $HfCl_4$ (0.200 g, 0.624 mmol) and $Li(PhBH_3)$ (0.244 g, 2.50 mmol). Yield: 167 mg

Open Access Article. Published on 29 October 2025. Downloaded on 2/23/2026 2:13:50 AM. This article is licensed under a Creative Commons Attribution-NonCommercial 3.0 Unported Licence.

(51%). M.p.: 130 °C (dec). Anal. calcd for $C_{24}H_{32}B_4Hf$: C, 53.16; H, 5.95. Found: C, 43.41; H, 5.32. $^1$H NMR (500 MHz, $C_6D_6$, $\delta$): 7.40–7.32 (m, 6H, CH), 7.272–7.17 (m, 14H, CH), 3.46 (br s, 12H, $BH_3$). $^{11}$B NMR (128 MHz, $C_6D_6$, $\delta$): −4.08 (br s, $BH_3$) IR (KBr) $\bar{\upsilon}_{max}$ ($cm^{-1}$) 3071 (m), 3051 (m), 3010 (m), 2967 (w), 2925 (w), 2369 (m), 2346 (m), 2147 (s), 2089 (s), 1604 (m), 1494 (w), 1434 (s), 1336 (s), 1304 (s), 1290 (s), 1170 (s), 1028 (s), 910 (w), 835 (s), 737 (vs), 696 (vs).

### Tetrakis(benzyltrihydroborato)zirconium(IV), [Zr(BnBH$_3$)$_4$]

Prepared as described for [Zr(PhBH$_3$)$_4$] with $ZrCl_4$ (0.200 g, 0.858 mmol) and Li/K(BnBH$_3$) (0.394 g, 3.52 mmol based on Li). Yield: 348 mg (79%). M.p.: 130 °C (dec). Anal. calcd for $C_{28}H_{40}B_4Zr$: C, 65.80; H, 7.89. Found (run 1): C, 54.09; H, 7.23. Found (run 2): C, 53.94; H, 6.90. Found (run 3): C, 52.58; H, 6.96. $^1$H NMR (500 MHz, $C_6D_6$, $\delta$): 7.21–7.13 (m, 6H, CH), 7.08–6.99 (m, 14H, CH), 2.09 (s, 8H, $CH_2$), 1.83 (br s, 12H, $BH_3$) $^{11}$B NMR (128 MHz, $C_6D_6$, $\delta$): −0.36 (br s, $BH_3$). IR (KBr) $\bar{\upsilon}_{max}$ ($cm^{-1}$) 3079 (m), 3068 (w), 3022 (s), 2962 (s), 2918 (s), 2895 (m), 2809 (w), 2130 (s), 2077 (s), 1894 (w), 1800 (w), 1744 (w), 1598 (s), 1492 (s), 1451 (s), 1414 (s), 1261 (s), 1177 (s), 1082 (s), 1027 (s), 900 (w), 799 (s), 746 (s), 696 (s).

### Tetrakis(benzyltrihydroborato)hafnium(IV), [Hf(BnBH$_3$)$_4$]

Prepared as described for [Zr(PhBH$_3$)$_4$] with $HfCl_4$ (0.200 g, 0.624 mmol) and Li/K(BnBH$_3$) (0.287 g, 2.56 mmol based on Li). Yield: 307 mg (82%). M.p.: 130 °C (dec). Anal. calcd for $C_{28}H_{40}B_4Hf$: C, 56.21; H, 6.74. Found (run 1): C, 51.43; H, 5.36. Found (run 2): C, 54.43; H, 5.46. Found (run 3): C, 52.36; H, 5.17. $^1$H NMR (500 MHz, $C_6D_6$, $\delta$): 7.21–7.14 (m, 6H, CH), 7.10–7.00 (m, 14H, CH), 2.49 (br s, 12H, $BH_3$), 2.04 (s, 8H, $CH_2$). $^{11}$B NMR (128 MHz, $C_6D_6$, $\delta$): −4.07 (br s. $BH_3$) IR (KBr) $\bar{\upsilon}_{max}$ ($cm^{-1}$) 3079 (m), 3060 (m), 3021 (s), 2920 (m), 2897 (m), 2811 (w), 2138 (s), 2093 (s), 1943 (w), 1867 (w), 1802 (w), 1745 (w), 1599 (vs), 1588 (m), 1491 (vs), 1451 (s), 1419 (w), 1283 (s), 1180 (s), 1084 (s), 1027 (w), 1003 (w), 902 (w), 77 (w), 748 (s), 695 (vs).

### Tetrakis(2,4,6-trimethylphenyltrihydroborato)zirconium(IV), [Zr(MesBH$_3$)$_4$]

Prepared as described for [Zr(PhBH$_3$)$_4$] with $ZrCl_4$ (0.104 g, 0.44 mmol) and Li(MesBH$_3$) (0.250 g, 1.8 mmol). Yield: 101 mg (36%). Anal. calcd for $C_{36}H_{56}B_4Zr$: C, 69.37; H, 9.06. Found: C, 56.51; H, 6.46. $^1$H NMR (500 MHz, $C_6D_6$, $\delta$): 6.82 (s, 8H, CH), 2.94 (br s, 12H, $BH_3$), 2.45 (s, 24H, $CH_3$), 2.19 (s, 12H, $CH_3$). $^{11}$B NMR (128 MHz, $C_6D_6$, $\delta$): −1.61 (s, $BH_3$). IR (Nujol) $\bar{\upsilon}_{max}$ ($cm^{-1}$): 2955 (s), 2925 (s), 2853 (s), 2144 (s), 2032 (s), 1605 (s), 1456 (s), 1377 (s), 1284 (m), 1177 (s), 1130 (s), 1039 (m), 846 (s), 802 (s), 718 (s).

### Tetrakis(2,4,6-trimethylphenyltrihydroborato)hafnium(IV), [Hf(MesBH$_3$)$_4$]

Prepared as described for [Zr(PhBH$_3$)$_4$] with $HfCl_4$ (0.147 g, 0.31 mmol) and Li(MesBH$_3$) (0.250 g, 1.8 mmol). Yield: 77.5 mg (16%). $^1$H NMR (500 MHz, $C_6D_6$, $\delta$): 6.85 (s, 8H, CH), 3.70 (br s, 12H, $BH_3$), 2.45 (s, 24H, $CH_3$), 2.19 (s, 12H, $CH_3$). $^{11}$B NMR (128 MHz, $C_6D_6$, , $\delta$): −3.67 (s, $BH_3$). IR (ATR) $\bar{\upsilon}_{max}$ ($cm^{-1}$): 2956 (s), 2908 (s), 2850 (s), 2139 (s), 2059 (s), 1606 (s), 1552 (s), 1436 (s), 1422 (s), 1300 (s), 1273 (s), 1236 (s), 1183 (s), 1133 (s), 1031 (s), 1011 (s), 955 (s), 919 (s), 546 (s), 801 (s), 717 (s), 686 (s).

### Tetrakis(2,4,6-triisopropylphenyltrihydroborato) zirconium(IV), [Zr(TripBH$_3$)$_4$]

Prepared as described for [Zr(PhBH$_3$)$_4$] with $ZrCl_4$ (0.104 g, 0.44 mmol) and Li(TripBH$_3$) (0.400 g, 1.8 mmol). Yield: 226 mg (53%). $^1$H NMR (300 MHz, $C_6D_6$, $\delta$): 7.14 (s, 8H, CH), 3.62 (sep, 8H, CH), 3.39 (br s, 12H, $BH_3$), 2.81 (sep, 4H, CH), 1.37–1.34 (d, 48H, $CH_3$), 1.25–1.22 (d, 24H, $CH_3$). $^{11}$B NMR (96 MHz, $C_6D_6$, , $\delta$): −0.81 (s, $BH_3$). IR (Nujol) $\bar{\upsilon}_{max}$ ($cm^{-1}$): 2955 (s), 2905 (s), 2853 (s), 2143 (s), 2031 (s), 1601 (s), 1554 (s), 1461 (s), 1377 (s), 1291 (s), 1251 (s), 1215 (s), 1191 (s), 1158 (s), 1109 (s), 1066 (s), 930 (s), 873 (s), 784 (s), 758 (s), 721 (s), 544 (s).

### Tetrakis(2,4,6-triisopropylphenyltrihydroborato)hafnium(IV), [Hf(TripBH$_3$)$_4$]

Prepared as described for [Zr(PhBH$_3$)$_4$] with $HfCl_4$ (0.143 g, 0.45 mmol) and Li(TripBH$_3$) (0.400 g, 1.8 mmol). Yield: 190 mg (47%). $^1$H NMR (300 MHz, $C_6D_6$, $\delta$): 7.18 (s, 8H, CH), 3.62 (sep, 8H, CH), 4.18 (br s, 12H, $BH_3$), 2.83 (sep, 4H, CH), 1.38–1.35 (d, 48H, $CH_3$), 1.26–1.24 (d, 24H, $CH_3$). $^{11}$B NMR (96 MHz, $C_6D_6$, , $\delta$): −3.31 (s, $BH_3$). IR (Nujol) $\bar{\upsilon}_{max}$ ($cm^{-1}$): 2956(s), 2925 (s), 2853 (s), 2153 (s), 2043 (s), 1601 (s), 1556 (s), 1458 (s), 1377 (s), 1292 (m), 1254 (s), 1159 (s), 1106 (s), 1068 (s), 930 (s), 873 (s), 783 (s), 757 (s), 721 (s), 520 (s).

### Tetrakis(9-anthryltrihydroborato)zirconium(IV), [Zr(AnthBH$_3$)$_4$]

$ZrCl_4$ (0.050 g, 0.21 mmol) and Li(AnthBH$_3$) (0.28 g, 0.83 mmol) were added to a 20 mL scintillation vial with pentane (20 mL), which resulted in a light green suspension. The suspension remained the same color after stirring overnight and the colorless pentane was decanted. After evaporating the pentane under reduced pressure, the green powder was extracted with toluene (2 × 20 mL) and filtered through a pad of Celite. The combined toluene extracts were evaporated to dryness under vacuum to reveal a green residue adhered to the sides of the vial. This residue was washed once with pentane (10 mL) and dissolved in toluene (5–8 mL). Vapor diffusion with pentane overnight afforded green needle-like crystals that were isolated by decanting the mother liquor and washing with pentane (5 mL). Yield: 73 mg (49%). $^1$H NMR (300 MHz, $C_6D_6$, $\delta$): 8.90 (d, 4H), 8.29 (s, 4H), 7.90 (d, 8H), 7.91 (m, 16H), 4.13 (br, s, 12H, $BH_3$). $^{11}$B NMR (96 MHz, $C_6D_6$, $\delta$): −0.46 (s, $BH_3$). IR (Nujol) $\bar{\upsilon}_{max}$ ($cm^{-1}$): 2921 (s), 2850 (s), 2150 (w), 2092 (w), 1508 (s), 1466 (s), 1375 (s), 1296 (s), 1216 (s), 889 (s), 839 (s), 734 (s).

### Tetrakis(9-anthryltrihydroborato)hafnium(IV), [Hf(AnthBH$_3$)$_4$]

Prepared as described for [Zr(AnthBH$_3$)$_4$] with $HfCl_4$ (0.076 g, 0.23 mmol) and Li(AnthBH$_3$) (0.32 g, 0.95 mmol). Vapor diffusion with pentane overnight afforded light green needle-like crystals that were isolated by decanting the mother liquor and washing with


© 2025 The Author(s). Published by the Royal Society of Chemistry

Open Access Article. Published on 29 October 2025. Downloaded on 2/23/2026 2:13:50 AM. This article is licensed under a Creative Commons Attribution-NonCommercial 3.0 Unported Licence.

pentane (5 mL). Yield: 18 mg (11%). $^1$H NMR (300 MHz, $C_6D_6$, $\delta$): 8.91 (d, 8H), 8.33 (s, 4H), 7.93 (d, 8H), 7.34 (m, 16H), 4.91 (br, s, 12H, $BH_3$) $^{11}$B NMR (96 MHz, $C_6D_6$, $\delta$): −2.89 (s, $BH_3$). IR (Nujol) $\bar{\upsilon}_{max}$ ($cm^{-1}$): 3044 (s), 2960 (s), 2175 (s), 2083 (s), 1619 (s), 1514 (s), 1451 (s), 1304 (s), 1238 (s), 1092 (s), 1021 (s), 954 (s), 883 (s), 837 (s), 806 (s), 783 (s), 752 (s), 721 (s), 646 (s), 606 (s).

### Single-crystal X-ray diffraction studies

Single crystals isolated from pentane/toluene were mounted on a MiTeGen MicroLoop with ParatoneN/NVH oil. The data were collected on a Bruker D8 Venture Duo equipped with a Bruker Photon III detector. The samples were cooled to 100 K with an Oxford Cryostreams 800 low-temperature device. All data were collected with a graphite monochromatized Mo K$\alpha$ X-ray source ($\lambda = 0.71073$). Data collections for each crystal were carried out using a mixture of phi and omega scans. The data collection, initial indexing, and cell refinement were conducted using the Bruker Apex6 suite. The data were corrected for absorption using redundant reflections and the SADABS program. Structure solution and refinement were performed in Olex2 using SHELXT and SHELXL. Hydrogen atoms bound to carbon atoms were idealized and refined using a riding model. Hydrogen atoms attached to boron were placed in idealized positions with B–H distances = 1.20 Å and tetrahedral angles. The $BH_3$ groups were allowed to rotate about the B–C bond to find the best orientation to maximize the sum of the difference densities at the three hydrogen positions. HKL reflections with error/esd values ± 10 were omitted from the models. The final refinement included anisotropic displacement parameters on all non-hydrogen atoms. Isotropic extinction parameters were not needed for the refinements. Crystallographic details are summarized in Table S1 in the SI.

### Boron K-edge X-ray absorption spectroscopy

B K-edge XAS data were collected at the Canadian Light Source (CLS) in Saskatoon, Saskatchewan, Canada at the Variable Line Spacing Plane Grating Monochromator (VLS-PGM) beamline. All measurements were performed in the Linear Horizontal Polarization mode using the high-energy grating (98–250 eV). The data were collected at room temperature in total fluorescence yield (TFY) mode using a microchannel plate (MCP) detector. Beamline slit sizes used for data collection were 100 × 100 μm. The sample chamber was maintained between $10^{-8}$ and $10^{-10}$ torr for all measurements. Data were normalized to the $I_0$ current measured using a nickel mesh (90% transmission) placed in front of the sample. The energy of the beamline was calibrated using the B K-edge of elemental boron at 188.0 eV. All data were collected at RT on at least three unique sample points to minimize beam-induced decomposition. Measurements were collected over the 184–210 eV energy range with a step size of *ca.* 0.1 eV and a dwell time of 1.0 second.

Samples were prepared at CLS in an Ar-filled glovebox with less than 1.0 ppm of $O_2$ and $H_2O$. Cu sample plates containing a thin strip of double-sided copper tape (SPI Supplies), mortars, pestles, sample plate covers, and glass jars were heated in a furnace at 150 °C for at least 90 min before being transferred to the glovebox antechamber and allowed to cool under vacuum. Single crystals of each complex were ground by hand in a mortar and pestle for 30–60 seconds. The pestle was used to paint the ground sample onto the Cu tape or press the sample into In foil that was cut to size and adhered to the Cu sample plate using the copper tape. The sample plate was then transported to the beamline under Ar in a sealed glass jar.

Sealed sample jars were loaded into the antechamber of a purge box attached to the beamline loading chamber. The box was configured so that the purge gas flowed into the main chamber on one side of the box and exited through a port on the other side of the box through a tube connected to the antechamber. This configuration allowed the purge gas to also pass through and purge the antechamber *via* an exit valve located on the top of the antechamber. The box was purged with argon for at least 20 min prior to loading the jars into the antechamber. The box was then purged through the antechamber for at least another 10 min prior to transferring the sample jars from the antechamber into the main chamber for loading. Samples were quickly transferred from the jars and placed in the sample loading trays taking care to minimize sample exposure to <1 min. Once loaded, the sample chamber was immediately evacuated to $10^{-6}$ torr so they could be transferred under vacuum to the main data collection chamber maintained at *ca.* $10^{-9}$ torr.

### Theoretical calculations

Density functional theory (DFT) and time-dependent density functional theory (TDDFT) calculations were performed as described previously using the Gaussian 09 computational chemistry suite.[83] All geometries were fully optimized, and the conformational space was thoroughly examined for any additional geometric minima. Initial optimizations were performed at the B3LYP-d3 level.[62,63] Zr and Hf were modeled with the effective core potential and uncontracted basis set of Hay and Wadt augmented with a set of f-orbital polarization functions collectively known as LANL08(f).[64,66,84] All other atoms were modeled with Pople's split-valence double-z 6-31G(d,p) plus polarization basis set.[67] Time-dependent density functional theory (TDDFT) calculations were combined with information on the charges, spin densities and relative orbital contributions from Mulliken population analysis[85] of the individual molecular orbitals from the ground state structures in order to simulate and interpret the XAS data.

## Author contributions

HMH: writing – original draft, investigation, formal analysis. JCZ, PAZ, JJS, EMA, MYY, DKU, LZ: investigation, writing – reviewing & editing. JMK, SRD: supervision, funding acquisition, formal analysis, writing – review & editing.

## Conflicts of interest

There are no conflicts to declare.

Open Access Article. Published on 29 October 2025. Downloaded on 2/23/2026 2:13:50 AM. This article is licensed under a Creative Commons Attribution-NonCommercial 3.0 Unported Licence.

## Data availability

CCDC 2463919, 2463920, 2463921, 2463922, 2463923, 2463924 and 2463925 contain the supplementary crystallographic data for this paper.[86a–g]

The data supporting this article have been included in the supporting information (SI). Supplementary information: molecular structures from single-crystal XRD studies; NMR and IR spectra; Full B K-edge XAS spectra and photodecomposition studies. Tabulated molecular orbital compositions and energies from DFT. *XYZ* coordinates of optimized structures. See DOI: **https://doi.org/10.1039/d5sc06254c**.

## Acknowledgements

HMH, PAZ, JJS, and SRD were supported by the NNSA under award DE-NA0004151. JCZ and SRD also thank the Laboratory Directed Research and Development (LDRD) program of Los Alamos National Laboratory under project number 20220518MFR for funding preliminary data collection efforts at the Canadian Light Source (CLS). MYY thanks the NSF for support (CHE-2247235). EMA and JMK thank the National Science Foundation (OAC-2346664) for the purchase of an upgraded supercomputer at Colgate University, which supported this work. XRD data were collected using the instrument supported by NSF CHE-1828117. Some of the NMR data were collected using the instrument supported by NSF CHE-2017828. We thank Benj Revis for preparing thick-walled glass ampules used to ship samples to CLS. Part of the research described in this paper was performed using beamline VLS-PGM at the Canadian Light Source, a national research facility of the University of Saskatchewan, which is supported by the Canada Foundation for Innovation (CFI), the Natural Sciences and Engineering Research Council (NSERC), the National Research Council (NRC), the Canadian Institutes of Health Research (CIHR), the Government of Saskatchewan, and the University of Saskatchewan.

## References

1 H. R. Hoekstra and J. J. Katz, Preparation and properties of the group IV-B metal borohydrides, *J. Am. Chem. Soc.*, 1949, **71**, 2488–2492.
2 P. H. Bird and M. R. Churchill, The crystal structure of zirconium(IV) borohydride (at –160°), *Chem. Commun.*, 1967, 403.
3 K. Hedberg and V. Plato, Electron-diffraction investigation of zirconium tetraborohydride, $Zr(BH_4)_4$, *Inorg. Chem.*, 1971, **10**, 590–594.
4 M. Ehemann and H. Nöth, Metallboranate und Boranatometallate. IV. Boranatokomplexe $M(BH_4)^{n-4+n}$ des Zirkoniums, Hafniums und Thoriums, *Z. Anorg. Allg. Chem.*, 1971, **386**, 87–101.
5 R. W. Broach, I. S. Chuang, T. J. Marks and J. M. Williams, Metrical characterization of tridentate tetrahydroborate ligation to a transition-metal ion. Structure and bonding in $Hf(BH_4)_4$ by single-crystal neutron diffraction, *Inorg. Chem.*, 1983, **22**, 1081–1084.
6 T. J. Marks and J. R. Kolb, Covalent transition metal, lanthanide, and actinide tetrahydroborate complexes, *Chem. Rev.*, 1977, **77**, 263–293.
7 M. L. Neidig, D. L. Clark and R. L. Martin, Covalency in f-element complexes, *Coord. Chem. Rev.*, 2013, **257**, 394–406.
8 G. Parkin, Representation of Three-Center–Two-Electron Bonds in Covalent Molecules with Bridging Hydrogen Atoms, *J. Chem.*, 2019, **96**, 2467–2475.
9 Z. Xu and Z. Lin, Transition metal tetrahydroborato complexes: an orbital interaction analysis of their structure and bonding, *Coord. Chem. Rev.*, 1996, **156**, 139–162.
10 M. Besora and A. Lledós, Coordination Modes and Hydride Exchange Dynamics in Transition Metal Tetrahydroborate Complexes, in *Contemporary Metal Boron Chemistry I: Borylenes, Boryls, Borane σ-Complexes*, ed. T. B. Marder and Z. Lin, Springer, Berlin Heidelberg, 2008, pp. 149–202.
11 E. R. Bernstein and T. A. Keiderling, Optical and magnetic resonance spectra of inorganic molecular crystals-uranium borohydride $[U(BH_4)_4]$ in hafnium borohydride $[Hf(BH_4)_4]$, *J. Chem. Phys.*, 1973, **59**, 2105–2122.
12 R. H. Banks and N. M. Edelstein, Synthesis and characterization of protactinium(IV), neptunium(IV), and plutonium(IV) borohydrides, *ACS Symp. Ser.*, 1980, **131**, 331–348.
13 K. Rajnak, R. H. Banks, E. Gamp and N. Edelstein, Analysis of the optical spectrum of neptunium borodeuteride $(Np(BD_4)_4)$ diluted in zirconium borodeuteride $(Zr(BD_4)_4)$ and the magnetic properties of neptunium borohydride $(Np(BH_4)_4)$ and neptunium methylborohydride $(Np(BH_3CH_3)_4)$, *J. Chem. Phys.*, 1984, **80**, 5951–5962.
14 K. Rajnak, E. Gamp, R. Banks, R. Shinomoto and N. Edelstein, Optical and magnetic properties of uranium and neptunium borohydrides and tetrakismethylborohydrides, *Inorg. Chim. Acta*, 1984, **95**, 29–35.
15 K. Rajnak, E. Gamp, R. Shinomoto and N. Edelstein, Optical and magnetic properties of uranium borohydride and tetrakismethylborohydride, *J. Chem. Phys.*, 1984, **80**, 5942–5950.
16 W. K. Kot and N. M. Edelstein, Protactinium chemistry: the synthesis and electronic structure of $Pa(BH_3CH_3)_4$, *New J. Chem.*, 1995, **19**, 641–654.
17 E. Gamp and N. Edelstein, Effects of small distortions on the EPR of the $\Gamma_6$ state ($T_d$ symmetry) of $Np(BH_3CH_3)_4$ diluted in $Zr(BH_3CH_3)_4$, *J. Chem. Phys.*, 1984, **80**, 5963–5967.
18 E. Gamp, R. Shinomoto, N. Edelstein and B. R. McGarvey, Multinuclear NMR spectroscopy of the tetrahedral uranium(IV) complex tetrakis(trihydromethylborato) uranium, *Inorg. Chem.*, 1987, **26**, 2177–2182.
19 B. R. McGarvey, Calculation of NMR paramagnetic shift temperature dependence in actinide methyl borohydrides, *Inorg. Chim. Acta*, 1998, **272**, 43–54.
20 A. J. Downs, R. G. Egdell, A. F. Orchard and P. D. P. Thomas, Photoelectron spectra of metal tetrahydroborates, *J. Chem. Soc., Dalton Trans.*, 1978, 1755–1761.


© 2025 The Author(s). Published by the Royal Society of Chemistry

Open Access Article. Published on 29 October 2025. Downloaded on 2/23/2026 2:13:50 AM. This article is licensed under a Creative Commons Attribution-NonCommercial 3.0 Unported Licence.

21 J. C. Green, M. de Simone, M. Coreno, A. Jones, H. M. I. Pritchard and G. S. McGrady, Electronic Structure of $M(BH_4)_4$, M = Zr, Hf, and U, by Variable Photon-Energy Photoelectron Spectroscopy and Density Functional Calculations, *Inorg. Chem.*, 2005, **44**, 7781–7793.

22 J. C. Green, R. Shinomoto and N. Edelstein, Photoelectron spectra of metal tetrakis(methyltrihydroborates) and thorium tetrakis(tetrahydroborate), *Inorg. Chem.*, 1986, **25**, 2718–2720.

23 D. B. Beach, K. D. Bomben, N. M. Edelstein, D. C. Eisenberg, W. L. Jolly, R. Shinomoto and A. Streitwieser Jr, An x-ray photoelectron spectroscopic study of uranium compounds, *Inorg. Chem.*, 1986, **25**, 1735–1737.

24 B. H. Thorsten Glaser, K. O. Hodgson and E. I. Solomon, Ligand K-edge X-ray Absorption Spectroscopy: A Direct Probe of Ligand-Metal Covalency, *Acc. Chem. Res.*, 2000, **33**, 859–868.

25 I. Edward, B. H. Solomon, K. O. Hodgson, A. Dey and R. K. Szilagyi, Ligand K-edge X-ray absorption spectroscopy: covalency of ligand-metal bonds, *Coord. Chem. Rev.*, 2005, **249**, 97–129.

26 O. Friedrichs, J. W. Kim, A. Remhof, D. Wallacher, A. Hoser, Y. W. Cho, K. H. Oh and A. Zuettel, Core-shell structure for solid gas synthesis of $LiBD_4$, *Phys. Chem. Chem. Phys.*, 2010, **12**, 4600–4603.

27 P. S. Miedema, P. Ngene, A. M. J. van der Eerden, T.-C. Weng, D. Nordlund, D. Sokaras, R. Alonso-Mori, A. Juhin, P. E. de Jongh and F. M. F. de Groot, In situ X-ray Raman spectroscopy of $LiBH_4$, *Phys. Chem. Chem. Phys.*, 2012, **14**, 5581–5587.

28 I. Saldan, J. M. Ramallo-Lopez, F. G. Requejo, K. Suarez-Alcantara, J. Bellosta von Colbe and J. Avila, NEXAFS study of 2LiF-$MgB_2$ composite, *Int. J. Hydrogen Energy*, 2012, **37**, 10236–10239.

29 P. S. Miedema, P. Ngene, A. M. J. van der Eerden, D. Sokaras, T.-C. Weng, D. Nordlund, Y. S. Au and F. M. F. de Groot, In situ X-ray Raman spectroscopy study of the hydrogen sorption properties of lithium borohydride nanocomposites, *Phys. Chem. Chem. Phys.*, 2014, **16**, 22651–22658.

30 A. Schneemann, L. F. Wan, A. S. Lipton, Y.-S. Liu, J. L. Snider, A. A. Baker, J. D. Sugar, C. D. Spataru, J. Guo, T. S. Autrey, M. Joergensen, T. R. Jensen, B. C. Wood, M. D. Allendorf and V. Stavila, Nanoconfinement of Molecular Magnesium Borohydride Captured in a Bipyridine-Functionalized Metal-Organic Framework, *ACS Nano*, 2020, **14**, 10294–10304.

31 R. Dahal, J. G. Vitillo, A. C. Aasland, C. Frommen, S. Deledda and O. Zavorotynska, X-ray and synchrotron Fourier-transform infrared spectroscopy studies of partially decomposed magnesium borohydride, *Energies*, 2022, **15**, 7998.

32 H. M. Hansen, P. Garg, J. J. Schuely, M. Y. Yang, O. K. Farha, J. M. Keith and S. R. Daly, Flash Communication: Boron K-edge XAS and TDDFT Studies of Covalent Metal-Ligand Bonding in $Ni(C_2B_9H_{11})_2$, *Organometallics*, 2025, **44**, 1624–1629.

33 B. Singaram, T. E. Cole and H. C. Brown, Addition compounds of alkali-metal hydrides. 25. Rapid reaction of boronic esters and acids with lithium aluminum hydride. A novel and quantitative synthesis of lithium monoorganylborohydrides, *Organometallics*, 1984, **3**, 774–777.

34 C. S. MacNeil, S.-J. Hsiang and P. G. Hayes, Reversible dehydrogenation of a primary aryl borane, *Chem. Commun.*, 2020, **56**, 12323–12326.

35 A. Pelter, K. Smith, D. Buss and Z. Jin, Hindered organoboron groups in organic synthesis. 17 [1]. Synthesis of 2,4,6-triisopropylphenylborane $(TripBH_2)_2$, a useful alternative to thexylborane, *Heteroat. Chem.*, 1992, **3**, 275–277.

36 Y. Wei, X. Yang, M. Tian, X. Wang and T. Wang, Ruthenium tris(σ-B–H) borate complexes: synthesis, structure, and reactivity, *Dalton Trans.*, 2022, **51**, 16354–16360.

37 C. M. Bateman, H. Beal, J. E. Barker, B. L. Thompson, D. Donovan, B. J. Grant, J. Shooter, J. H. Arakawa, S. Johnson, C. J. Allen, J. L. Yates, R. Kato, C. W. K. Tinsley, L. N. Zakharov and E. R. Abbey, One-Step Conversion of Potassium Organotrifluoroborates to Metal Organoborohydrides, *Org. Lett.*, 2018, **20**, 3784–3787.

38 See SI for representative NMR data for $Li(MesBH_3)$ in thf-$d_8$.

39 J. A. Jensen, J. E. Gozum, D. M. Pollina and G. S. Girolami, Titanium, zirconium, and hafnium tetrahydroborates as "tailored" CVD precursors for metal diboride thin films, *J. Am. Chem. Soc.*, 1988, **110**, 1643–1644.

40 E. Ding, B. Du, F.-C. Liu, S. Liu, E. A. Meyers and S. G. Shore, Preparation and Crystal Structures of a Series of Titanium(III) 9-BBN Hydroborate Complexes Containing Ti···H Agostic Interactions, *Inorg. Chem.*, 2005, **44**, 4871–4878.

41 S. R. Daly, P. M. B. Piccoli, A. J. Schultz, T. K. Todorova, L. Gagliardi and G. S. Girolami, Synthesis and properties of a fifteen-coordinate complex: the thorium aminodiboranate $[Th(H_3BNMe_2BH_3)_4]$, *Angew. Chem., Int. Ed.*, 2010, **49**, 3379–3381.

42 R. Shinomoto, E. Gamp, N. M. Edelstein, D. H. Templeton and A. Zalkin, Syntheses and crystal structures of the tetrakis(methyltrihydroborato) compounds of zirconium(IV), thorium(IV), uranium(IV), and neptunium(IV), *Inorg. Chem.*, 1983, **22**, 2351–2355.

43 U. Welling, P. Paetzold and U. Englert, Molecular and crystal structure of zirconium hydroborates, *Inorg. Chim. Acta*, 1995, **231**, 175–180.

44 F.-C. Liu, C.-C. Yang, S.-C. Chen, G.-H. Lee and S.-M. Peng, Novel $\mu_3$-oxo complexes prepared from $Cp^*Zr(BH_3R)_3$ (R = H, $CH_3$) and $B(C_6F_5)_3$ in diethyl ether, *Dalton Trans.*, 2008, 3599–3604.

45 F.-C. Liu, J.-H. Chen, S.-C. Chen, K.-Y. Chen, G.-H. Lee and S.-M. Peng, Syntheses, structures, and properties of phenyltrihydroborate complexes of zirconocene and titanocene, *J. Organomet. Chem.*, 2005, **690**, 291–300.

46 L. Yang, D. R. Powell and R. P. Houser, Structural variation in copper(I) complexes with pyridylmethylamide ligands:

Open Access Article. Published on 29 October 2025. Downloaded on 2/23/2026 2:13:50 AM. This article is licensed under a Creative Commons Attribution-NonCommercial 3.0 Unported Licence.

structural analysis with a new four-coordinate geometry index, *Dalton Trans.*, 2007, 955–964.

47 K. Burkmann, F. Habermann, E. Schumann, J. Kraus, B. Stoerr, H. Schmidt, E. Brendler, J. Seidel, K. Bohmhammel, J. Kortus and F. Mertens, Structural and thermodynamic investigations of $Zr(BH_4)_4$ and $Hf(BH_4)_4$ between 280 K and their decomposition temperatures, *New J. Chem.*, 2024, **48**, 2743–2754.

48 N. Davies, M. G. H. Wallbridge, B. E. Smith and B. D. James, Vibrational spectra of zirconium tetrahydroborate and related molecules, *J. Chem. Soc., Dalton Trans.*, 1973, 162–165.

49 T. A. Keiderling, W. T. Wozniak, R. S. Gay, D. Jurkowitz, E. R. Bernstein, S. J. Lippard and T. G. Spiro, Raman and infrared spectra of hafnium tetrakis(tetrahydroborate) and hafnium tetrakis(tetrahydroborate-$d_{16}$). Evidence for hafnium-boron bonding, *Inorg. Chem.*, 1975, **14**, 576–579.

50 T. J. Marks, W. J. Kennelly, J. R. Kolb and L. A. Shimp, Structure and dynamics in metal tetrahydroborates. II. Vibrational spectra and structures of some transition metal and actinide tetrahydroborates, *Inorg. Chem.*, 1972, **11**, 2540–2546.

51 T. W. Hayton and J. Autschbach, Using NMR Spectroscopy to Evaluate Metal–Ligand Bond Covalency for the f Elements, *Acc. Chem. Res.*, 2025, **58**, 488–498.

52 D. Hohl and N. Roesch, On the electronic structure of metal tetrahydroborates: quasi-relativistic Xα-SW study of $M(BH_4)_4$ (M = zirconium, hafnium, thorium, uranium), *Inorg. Chem.*, 1986, **25**, 2711–2718.

53 Y. F. Hu, L. Zuin, G. Wright, R. Igarashi, M. McKibben, T. Wilson, S. Y. Chen, T. Johnson, D. Maxwell, B. W. Yates, T. K. Sham and R. Reininger, Commissioning and performance of the variable line spacing plane grating monochromator beamline at the Canadian Light Source, *Rev. Sci. Instrum.*, 2007, **78**, 083109.

54 M. E. Fleet and S. Muthupari, Boron K-edge XANES of borate and borosilicate minerals, *Am. Mineral.*, 2000, **85**, 1009–1021.

55 J. G. Chen, NEXAFS investigations of transition metal oxides, nitrides, carbides, sulfides and other interstitial compounds, *Surf. Sci. Rep.*, 1997, **30**, 1–152.

56 D. Li, G. M. Bancroft and M. E. B. Fleet, K.-edge XANES of crystalline and amorphous inorganic materials, *J. Electron Spectrosc. Relat. Phenom.*, 1996, **79**, 71–73.

57 M. Magnuson, L. Tengdelius, G. Greczynski, L. Hultman and H. Högberg, Chemical bonding in epitaxial $ZrB_2$ studied by X-ray spectroscopy, *Thin Solid Films*, 2018, **649**, 89–96.

58 S. A. Kozimor, P. Yang, E. R. Batista, K. S. Boland, C. J. Burns, C. N. Christensen, D. L. Clark, S. D. Conradson, P. J. Hay, J. S. Lezama, R. L. Martin, D. E. Schwarz, M. P. Wilkerson and L. E. Wolfsberg, Covalency Trends in Group IV Metallocene Dichlorides. Chlorine K-Edge X-Ray Absorption Spectroscopy and Time Dependent-Density Functional Theory, *Inorg. Chem.*, 2008, **47**, 5365–5371.

59 S. A. Kozimor, P. Yang, E. R. Batista, K. S. Boland, C. J. Burns, D. L. Clark, S. D. Conradson, R. L. Martin, M. P. Wilkerson and L. E. Wolfsberg, Trends in Covalency for d- and f-Element Metallocene Dichlorides Identified Using Chlorine K-Edge X-ray Absorption Spectroscopy and Time-Dependent Density Functional Theory, *J. Am. Chem. Soc.*, 2009, **131**, 12125–12136.

60 S. G. Minasian, J. M. Keith, E. R. Batista, K. S. Boland, D. L. Clark, S. D. Conradson, S. A. Kozimor, R. L. Martin, D. E. Schwarz, D. K. Shuh, G. L. Wagner, M. P. Wilkerson, L. E. Wolfsberg and P. Yang, Determining Relative f and d Orbital Contributions to M-Cl Covalency in $MCl_6^{2-}$ (M = Ti, Zr, Hf, U) and $UOCl_5^-$ Using Cl K-edge X-ray Absorption Spectroscopy and Time-Dependent Density Functional Theory, *J. Am. Chem. Soc.*, 2012, **134**, 5586–5597.

61 S. G. Minasian, J. M. Keith, E. R. Batista, K. S. Boland, S. A. Kozimor, R. L. Martin, D. K. Shuh, T. Tyliszczak and L. J. Vernon, Carbon K-Edge X-ray Absorption Spectroscopy and Time-Dependent Density Functional Theory Examination of Metal-Carbon Bonding in Metallocene Dichlorides, *J. Am. Chem. Soc.*, 2013, **135**, 14731–14740.

62 A. D. Becke, Density-functional thermochemistry. III. The role of exact exchange, *J. Chem. Phys.*, 1993, **98**, 5648–5652.

63 S. Grimme, J. Antony, S. Ehrlich and H. Krieg, A consistent and accurate *ab initio* parametrization of density functional dispersion correction (DFT-D) for the 94 elements H-Pu, *J. Chem. Phys.*, 2010, **132**, 154104.

64 P. J. Hay and W. R. Wadt, Ab initio effective core potentials for molecular calculations. Potentials for potassium to gold including the outermost core orbitals, *J. Chem. Phys.*, 1985, **82**, 299–310.

65 A. W. Ehlers, M. Boehme, S. Dapprich, A. Gobbi, A. Hoellwarth, V. Jonas, K. F. Koehler, R. Stegmann and A. Veldkamp, A set of f-polarization functions for pseudopotential basis sets of the transition metals Sc-Cu, Y-Ag and La-Au, *Chem. Phys. Lett.*, 1993, **208**, 111–114.

66 L. E. Roy, P. J. Hay and R. L. Martin, Revised Basis Sets for the LANL Effective Core Potentials, *J. Chem. Theory Comput.*, 2008, **4**, 1029–1031.

67 R. Ditchfield, W. J. Hehre and J. A. Pople, Self-consistent molecular-orbital methods. IX. Extended Gaussian-type basis for molecular-orbital studies of organic molecules, *J. Chem. Phys.*, 1971, **54**, 724–728.

68 S. R. Daly, J. M. Keith, E. R. Batista, K. S. Boland, D. L. Clark, S. A. Kozimor and R. L. Martin, Sulfur K-edge X-ray Absorption Spectroscopy and Time-Dependent Density Functional Theory of Dithiophosphinate Extractants: Minor Actinide Selectivity and Electronic Structure Correlations, *J. Am. Chem. Soc.*, 2012, **134**, 14408–14422.

69 S. R. Daly, J. M. Keith, E. R. Batista, K. S. Boland, S. A. Kozimor, R. L. Martin and B. L. Scott, Probing Ni $[S_2PR_2]_2$ Electronic Structure to Generate Insight Relevant to Minor Actinide Extraction Chemistry, *Inorg. Chem.*, 2012, **51**, 7551–7560.

70 S. G. Minasian, J. M. Keith, E. R. Batista, K. S. Boland, D. L. Clark, S. D. Conradson, S. A. Kozimor, R. L. Martin, D. E. Schwarz, D. K. Shuh, G. L. Wagner, M. P. Wilkerson, L. E. Wolfsberg and P. Yang, Determining relative f and d orbital contributions to M-Cl covalency in $MCl_6^{2-}$ (M = Ti, Zr, Hf, U) and $UOCl_5^-$ using Cl K-Edge X-ray absorption


© 2025 The Author(s). Published by the Royal Society of Chemistry

Open Access Article. Published on 29 October 2025. Downloaded on 2/23/2026 2:13:50 AM. This article is licensed under a Creative Commons Attribution-NonCommercial 3.0 Unported Licence.

spectroscopy and time-dependent density functional theory, *J. Am. Chem. Soc.*, 2012, **134**, 5586–5597.

71 S. G. Minasian, J. M. Keith, E. R. Batista, K. S. Boland, J. A. Bradley, S. R. Daly, S. A. Kozimor, W. W. Lukens, R. L. Martin, D. Nordlund, G. T. Seidler, D. K. Shuh, D. Sokaras, T. Tyliszczak, G. L. Wagner, T.-C. Weng and P. Yang, Covalency in Metal-Oxygen Multiple Bonds Evaluated Using Oxygen K-edge Spectroscopy and Electronic Structure Theory, *J. Am. Chem. Soc.*, 2013, **135**, 1864–1871.

72 C. M. Donahue, J. S. Lezama Pacheco, J. M. Keith and S. R. Daly, Sulfur K-edge X-ray Absorption Spectroscopy and Time-Dependent Density Functional Theory of Arsenic Dithiocarbamates, *Dalton Trans.*, 2014, **43**, 9189–9201.

73 C. M. Donahue, S. P. McCollom, C. M. Forrest, A. V. Blake, B. J. Bellott, J. M. Keith and S. R. Daly, Impact of Coordination Geometry, Bite Angle, and Trans Influence on Metal-Ligand Covalency in Phenyl-Substituted Phosphine Complexes of Ni and Pd, *Inorg. Chem.*, 2015, **54**, 5646–5659.

74 K. Lee, H. Wei, A. V. Blake, C. M. Donahue, J. M. Keith and S. R. Daly, Ligand K-edge XAS, DFT, and TDDFT Analysis of Pincer Linker Variations in Rh(I) PNP Complexes: Reactivity Insights from Electronic Structure, *Dalton Trans.*, 2016, **45**, 9774–9785.

75 A. V. Blake, H. Wei, C. M. Donahue, K. Lee, J. M. Keith and S. R. Daly, Solid Energy Calibration Standards for P K-edge XANES: Electronic Structure Analysis of $PPh_4Br$, *J. Synchrotron Radiat.*, 2018, **25**, 529–536.

76 A. V. Blake, H. Wei, K. Lee, C. M. Donahue, J. M. Keith and S. R. Daly, Solution and Solid-State Ligand K-Edge XAS Studies of $PdCl_2$ Diphosphine Complexes with Phenyl and Cyclohexyl Substituents, *Eur. J. Inorg. Chem.*, 2018, **2018**, 2267–2276.

77 K. Lee, H. Wei, A. V. Blake, C. M. Donahue, J. M. Keith and S. R. Daly, Measurement of Diphosphine σ-Donor and π-Acceptor Properties in $d^0$ Titanium Complexes Using Ligand K-Edge XAS and TDDFT, *Inorg. Chem.*, 2018, **57**, 10277–10286.

78 K. Lee, A. V. Blake, C. M. Donahue, K. D. Spielvogel, B. J. Bellott and S. R. Daly, Quantifying the Interdependence of Metal-Ligand Covalency and Bond Distance using Ligand K-edge XAS, *Angew. Chem., Int. Ed.*, 2019, **58**, 12451–12455.

79 K. Lee, A. V. Blake, A. Tanushi, S. M. McCarthy, D. Kim, S. M. Loria, C. M. Donahue, K. D. Spielvogel, J. M. Keith, S. R. Daly and A. T. Radosevich, Validating the Biphilic Hypothesis of Nontrigonal Phosphorus(III) Compounds, *Angew. Chem., Int. Ed.*, 2019, **58**, 6993–6998.

80 R. D. Shannon, Revised effective ionic radii and systematic studies of interatomic distances in halides and chalcogenides, *Acta Crystallogr., Sect. A*, 1976, **A32**, 751–767.

81 R. Dennington, T. A. Keith and J. M. Millam, *GaussView*, Version 5, Semichem Inc., Shawnee Mission, KS, 2008.

82 J. C. Zgrabik, P. A. Zacher III and S. R. Daly, f-Element complexes with benzyl and cyclohexyl substituted trihydroborates, *Polyhedron*, 2025, **269**, 117408.

83 M. J. Frisch, G. W. Trucks, H. B. Schlegel, G. E. Scuseria, M. A. Robb, J. R. Cheeseman, G. Scalmani, V. Barone, G. A. Petersson, H. Nakatsuji, X. Li, M. Caricato, A. V. Marenich, J. Bloino, B. G. Janesko, R. Gomperts, B. Mennucci, H. P. Hratchian, J. V. Ortiz, A. F. Izmaylov, J. L. Sonnenberg, D. Williams-Young, F. Ding, F. Lipparini, F. Egidi, J. Goings, B. Peng, A. Petrone, T. Henderson, D. Ranasinghe, V. G. Zakrzewski, J. Gao, N. Rega, G. Zheng, W. Liang, M. Hada, M. Ehara, K. Toyota, R. Fukuda, J. Hasegawa, M. Ishida, T. Nakajima, Y. Honda, O. Kitao, H. Nakai, T. Vreven, K. Throssell, J. A. Montgomery Jr, J. E. Peralta, F. Ogliaro, M. J. Bearpark, J. J. Heyd, E. N. Brothers, K. N. Kudin, V. N. Staroverov, T. A. Keith, R. Kobayashi, J. Normand, K. Raghavachari, A. P. Rendell, J. C. Burant, S. S. Iyengar, J. Tomasi, M. Cossi, J. M. Millam, M. Klene, C. Adamo, R. Cammi; J. W. Ochterski, R. L. Martin, K. Morokuma, O. Farkas, J. B. Foresman, D. J. Fox, *Gaussian 16, Revision C.01*, Gaussian, Inc., Wallingford CT, 2016.

84 A. W. Ehlers, M. Boehme, S. Dapprich, A. Gobbi, A. Hoellwarth, V. Jonas, K. F. Koehler, R. Stegmann, A. Veldkamp, *et al.*, A set of f-polarization functions for pseudopotential basis sets of the transition metals Sc-Cu, Y-Ag and La-Au, *Chem. Phys. Lett.*, 1993, **208**, 111–114.

85 R. S. Mulliken, Electronic population analysis on LCAO-MO [linear combination of atomic orbital-molecular orbital] molecular wave functions. I, *J. Chem. Phys.*, 1955, **23**, 1833–1840.

86 (*a*) CCDC 2463919: Experimental Crystal Structure Determination, 2025, DOI: **10.5517/ccdc.csd.cc2npx8k**; (*b*) CCDC 2463920: Experimental Crystal Structure Determination, 2025, DOI: **10.5517/ccdc.csd.cc2npx9l**; (*c*) CCDC 2463921: Experimental Crystal Structure Determination, 2025, DOI: **10.5517/ccdc.csd.cc2npxbm**; (*d*) CCDC 2463922: Experimental Crystal Structure Determination, 2025, DOI: **10.5517/ccdc.csd.cc2npxcn**; (*e*) CCDC 2463923: Experimental Crystal Structure Determination, 2025, DOI: **10.5517/ccdc.csd.cc2npxdp**; (*f*) CCDC 2463924: Experimental Crystal Structure Determination, 2025, DOI: **10.5517/ccdc.csd.cc2npxfq**; (*g*) CCDC 2463925: Experimental Crystal Structure Determination, 2025, DOI: **10.5517/ccdc.csd.cc2npxgr**.